SANDIA REPORT

SAND2004-2864
Unlimited Release
Printed June 2004

Multi-dimensional Multi-species Modeling of Transient Electrodeposition in LIGA Microfabrication

Ken S. Chen and Gregory H. Evans

Prepared by
Sandia National Laboratories
Albuquerque, New Mexico 87185 and Livermore, California 94550

Sandia is a multiprogram laboratory operated by Sandia Corporation,
a Lockheed Martin Company, for the United States Department of Energy's
National Nuclear Security Administration under Contract DE-AC04-94AL85000.

Issued by Sandia National Laboratories, operated for the United States Department of Energy by Sandia Corporation.

Available to DOE and DOE contractors from
U.S. Department of Energy
Office of Scientific and Technical Information
P.O. Box 62
Oak Ridge, TN 37831

Telephone: (865)576-8401
Facsimile: (865)576-5728
E-Mail: reports@adonis.osti.gov
Online ordering: http://www.osti.gov/bridge

Available to the public from
U.S. Department of Commerce
National Technical Information Service
5285 Port Royal Rd
Springfield, VA 22161

Telephone: (800)553-6847
Facsimile: (703)605-6900
E-Mail: orders@ntis.fedworld.gov
Online order: http://www.ntis.gov/help/ordermethods.asp?loc=7-4-0#online

SAND2004-2864
Unlimited Release
Printed June 2004

Multi-dimensional Multi-species Modeling of Transient Electrodeposition in LIGA Microfabrication

Ken S. Chen* and Gregory H. Evans** *
Multiphase Transport Processes Department
Sandia National Laboratories
P.O. Box 5800 Albuquerque, New Mexico 87185-0834
** Fluid and Thermal Science Department
Sandia National Laboratories
Livermore, CA 94550-9042

Abstract

This report documents the efforts and accomplishments of the LIGA electrodeposition modeling project which was funded by the ASCI Materials and Physics Modeling Program. A multi-dimensional framework based on GOMA was developed for modeling time-dependent diffusion and migration of multiple charged species in a dilute electrolyte solution with reduction electro-chemical reactions on moving deposition surfaces. By combining the species mass conservation equations with the electroneutrality constraint, a Poisson equation that explicitly describes the electrolyte potential was derived. The set of coupled, nonlinear equations governing species transport, electric potential, velocity, hydrodynamic pressure, and mesh motion were solved in GOMA, using the finite-element method and a fully-coupled implicit solution scheme via Newton's method. By treating the finite-element mesh as a pseudo solid with an arbitrary Lagrangian-Eulerian formulation and by repeatedly performing re-meshing with CUBIT and re-mapping with MAPVAR, the moving deposition surfaces were tracked explicitly from start of deposition until the trenches were filled with metal, thus enabling the computation of local current densities that potentially influence the microstructure and functional/mechanical properties of the deposit. The multi-dimensional, multi-species, transient computational framework was demonstrated in case studies of two-dimensional nickel electrodeposition in single and multiple trenches, without and with bath stirring or forced flow. Effects of buoyancy-induced convection on deposition were also investigated. To further illustrate its utility, the framework was employed to simulate deposition in microscreen-based LIGA molds. Lastly, future needs for modeling LIGA electrodeposition are discussed.

Acknowledgment

This project was funded entirely by the Materials and Physics Modeling Program within ASCI (the Accelerated Scientific Computing Initiative). We would like to thank Bob Nilson (8752) and Stewart Griffiths (8750) for helpful discussions on LIGA electrodeposition. Discussions with Rich Larson (8752) and Prof. Ralph Greif (UC Berkeley) on modeling electrodeposition were very helpful. We also want to thank Randy Schunk (9114) and other members of the GOMA team for various discussions related to GOMA. We wish to acknowledge the contributions by Prof. Branko N. Popov of the University of South Carolina on the study of nickel-plating-bath solution chemistry and the nickel-plating data for model validation. Assistance by summer student intern, Justin O'Neal, in our modeling-validation work is also appreciated.

Contents

1 Introduction

In recent years LIGA (LIthographie, Galvanoformung, Abformung, which are German words for lithography, electroplating and molding) is increasingly demonstrated to be a viable technology in fabrication of micro-devices or parts (see, e.g., Hruby 2001). Electrodeposition is a key process in LIGA microfabrication, which consists of three essential steps as depicted in Figure 1: i) exposing non-conducting PMMA (polymethyl-methacrylate) molds by deep or high-energy x-ray lithography; ii) removing the exposed PMMA in a developer bath to produce feature cavities or trenches; and iii) filling the feature trenches with a desired metal such as nickel or an alloy such as nickel-cobalt-iron. The widths of the feature trenches can be as small as ten microns or less whereas the depths are on the order of hundreds to thousands of microns – this means that the resultant aspect ratio is high. Understanding how depositing metal ions are transported from the electrolyte bath to the bottom surfaces of the trenches is a key in fabricating quality LIGA parts that possess the desired and uniform functional and mechanical properties. In a LIGA electrodeposition process, an external voltage is applied between the target-metal anode and the metal-deposit cathode under constant load or current density. To keep the electrolyte solution well mixed and to shorten deposition time, the electrolyte bath is usually stirred. Several sample test structures and parts made at Sandia by LIGA microfabrication are shown in Figures 2 – 4.

Pioneering work of modeling LIGA electrodeposition was carried out by Griffiths et al. (1998a, 1998b), who developed one- and two-dimensional numerical models describing electrodeposition of metal into high aspect-ratio molds. On the one hand, their one-dimensional model describes dissociation, diffusion, electromigration, and deposition of multiple ionic species. One the other hand, their two-dimensional model focuses on single-species transport including forced flow due to bath stirring and buoyancy-induced natural convection due to density variations. However, none of the prior work addresses all of these phenomena within a single fully-coupled framework and there has been no prior modeling of the transient and moving boundary effects of importance in LIGA. More recently, Nilson and Griffiths (2003) reported their study of transport enhancement by buoyancy-driven convection induced by metal-ion depletion adjacent to the plating surface. They found that significant transport enhancement may be achieved during electrodeposition into features having depths greater than about 100 μm and that "enhancement exceeding a factor of ten may occur in LIGA features having depths of 1 mm or more". Hayashi et al. (2001) reported (based on their experimental observations) that the natural convection due to density difference is effective in stirring the inside of cavity with 200 μm width but "the natural convection is not effective for cavities smaller than 100 μm in width". Although these studies demonstrate the importance of convection, there has been no prior modeling of the effects of convection on the shape of the evolving electrodeposit.

Our efforts were motivated by the generally accepted view that computational modeling can help to improve the understanding of these complex, coupled phenomena and aid in elucidating the mechanisms involved in LIGA electrodeposition. Specifically, by computing local current densities along the moving deposition surfaces, one can potentially relate deposit microstructure (which controls the functional and mechanical properties of the structure) to process conditions (e.g., applied current load, bath compo-

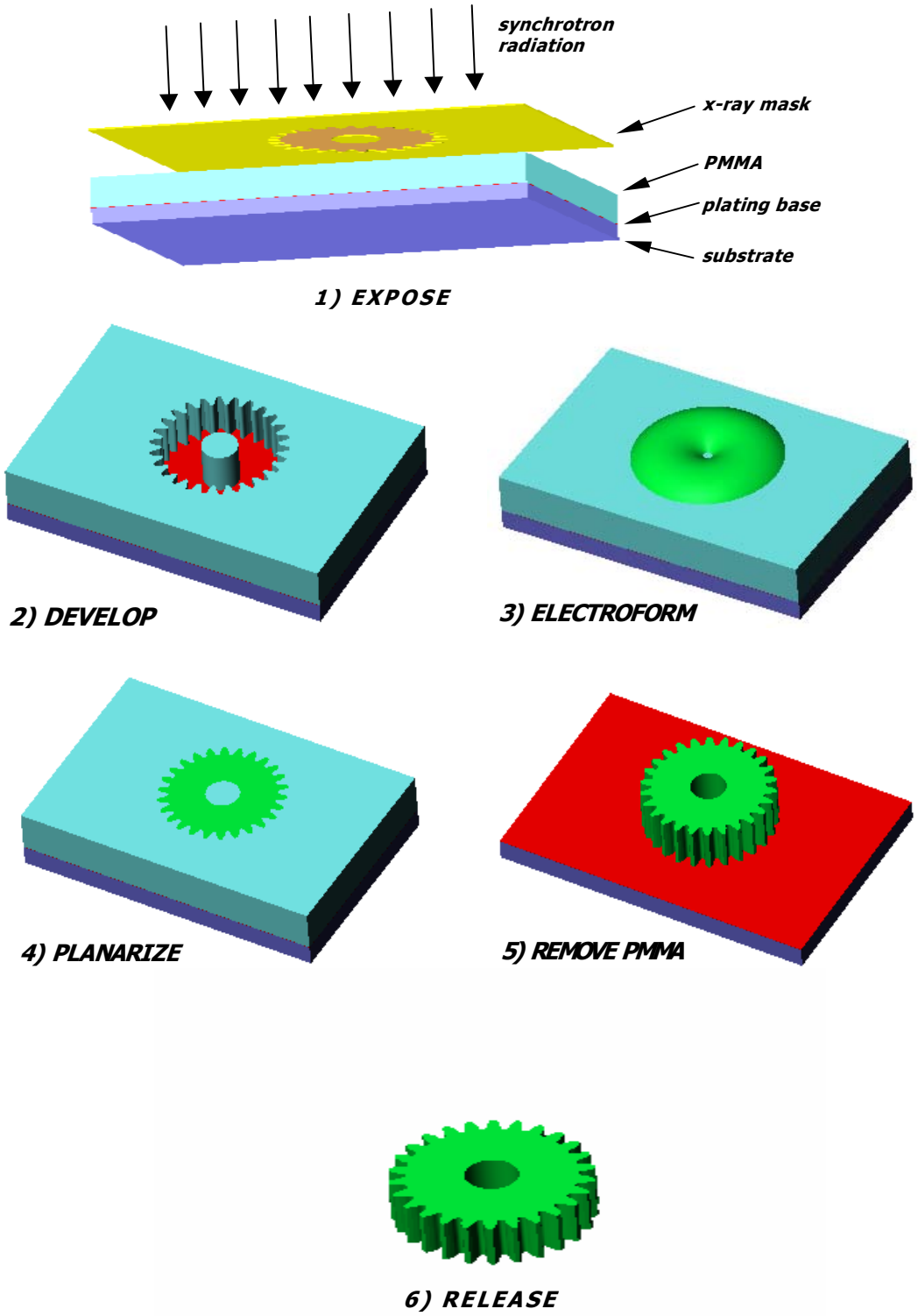

Figure 1. Steps involved in a typical LIGA microfabrication process (Christenson 2000).

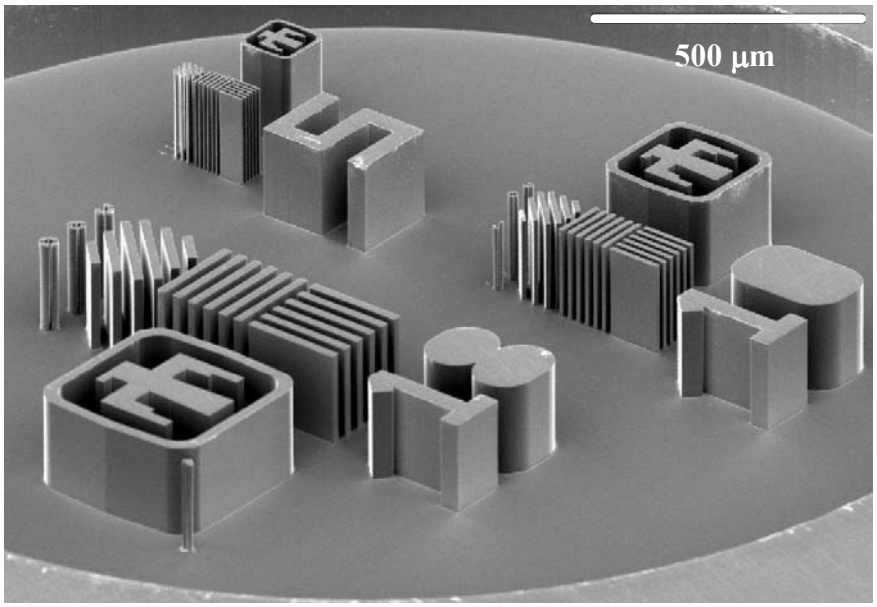

(a)

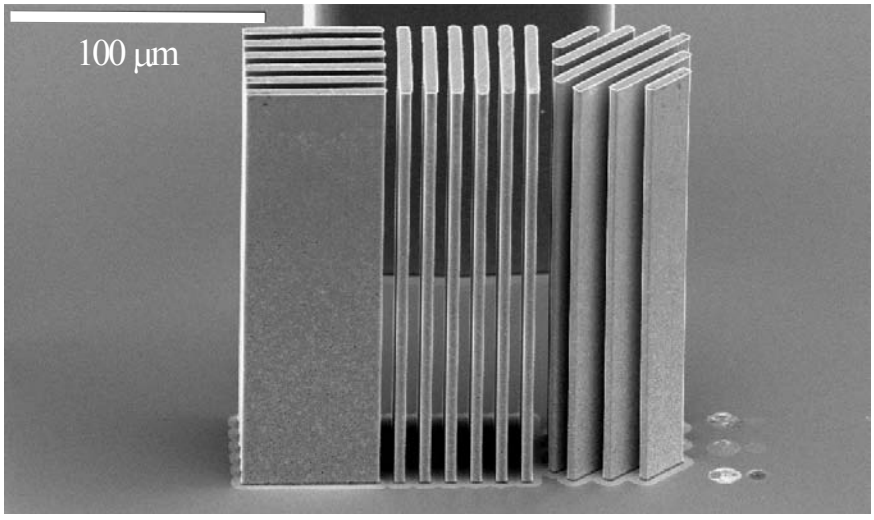

(b)

Figure 2. Sample test structures made by direct LIGA microfabrication (Chrsitenson 2000).
(a) 200 μm tall nickel structures;
(b) close-up of 5 μm nickel lines and spaces

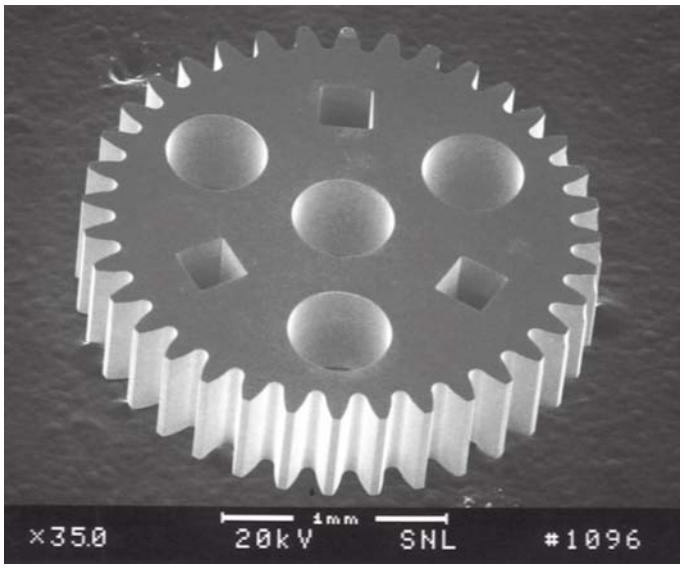

Figure 3. More sample part made by direct LIGA microfabrication – micro gear (Christenson 2000).

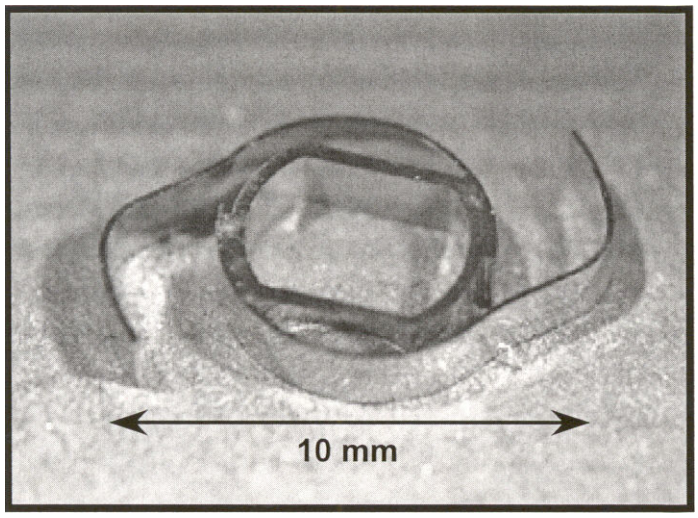

Figure 4. Contact spring made from LIGA microfabrication (Good et al. 2003).

sition, pH, and temperature) and trench geometries (widths, aspect ratios), provided that constitutive models relating current density to microstructure (e.g., grain size and orientation) and microstructure to functional/mechanical properties are available.

In the present work, we developed a multi-dimensional framework based on GOMA (a multi-physics multi-dimensional finite-element computer code developed and being enhanced at Sandia National Laboratories; see Schunk et al. 1997, 2002) for modeling time-dependent diffusion and migration of multiple charged species in a dilute electrolyte solution with reduction electrochemical reactions on moving deposition surfaces. By

combining the species mass conservation equations with the electroneutrality constraint, a Poisson equation that explicitly describes the electrolyte potential was derived. The set of coupled, nonlinear equations governing species concentration, electric potential, velocity, hydrodynamic pressure, and mesh motion were solved in GOMA, using the finite-element method and a fully-coupled implicit solution scheme via Newton's method. By treating the finite-element mesh as a pseudo solid with an arbitrary Lagrangian-Eulerian formulation and by repeatedly performing re-meshing with CUBIT (a meshing toolkit developed at Sandia; see CUBIT website at http://sass1693.Sandia.gov/cubit) and re-mapping with MAPVAR (a Sandia-developed utility program, see Wellman 1999), the moving deposition surfaces were tracked explicitly from start of deposition until the trenches were filled with metal, thus enabling the computation of local current densities that influence the microstructure and functional/mechanical properties of the deposit. The multi-dimensional, multi-species, transient computational framework was demonstrated in case studies of two-dimensional nickel electrodeposition in single and multiple trenches, without and with bath stirring or forced flow. Effects of buoyancy-induced convection on deposition were also investigated. To further illustrate its utility, the framework was employed to simulate deposition in microscreen-based LIGA molds. Lastly, future needs for modeling LIGA electrodeposition are discussed.

Portions of the work documented here have been reported elsewhere (Chen 2003, Chen and Evans 2004, Evans et al. 2002). In the following, governing equations are presented and numerical solution methods discussed in Section 2. Computational results of several case studies are documented in Section 3. We summarize our efforts and accomplishments, and provide comments on future work in Section 4. Lastly, a study of solution chemistry of Watts nickel plating bath in the absence of additives and deposition mechanism is attached as the Appendix. This study was carried out by our collaborator, Prof. Branko Popov, at the University of South Carolina as part of a contract project with Sandia (Popov 2002).

2 Governing Equations and Numerical Solution Methods

2.1 Species concentrations

Concentrations of individual species are described by the law of species mass conservation with the aqueous electrolyte solution being treated as an incompressible fluid, i.e., $\nabla \cdot \mathbf{u} = 0$ (cf. Schunk et al. 1997, and Newman 1991):

$$\frac{dc_i}{dt} + (\mathbf{u} - \mathbf{u}_m) \cdot \nabla c_i + \nabla \cdot \mathbf{J}_i = r_i \qquad (1)$$

for i =1,..., (n-1) with n being the total number of species; c_i is the concentration of species i, t is time, $\mathbf{u}$ is the mixture velocity, $\mathbf{u_m}$ is the mesh velocity, d/dt ($\equiv \partial/\partial$t + $\mathbf{u_m}\cdot\nabla$) is the total time derivative, and r_i is the net rate of generation or consumption from homogeneous electrochemical reactions for species i. In Equation 1, $\mathbf{J_i}$ are the combined

diffusive and migration fluxes, which are given by, for *dilute* electrolyte solutions (cf. Newman 1991):

$$\mathbf{J}_i = -D_i \nabla c_i - \frac{F}{RT} z_i D_i c_i \nabla \Phi \qquad (2)$$

where D_i and z_i are the diffusivity and charge number of species i, respectively; F is Faraday constant, R is universal gas constant, T is electrolyte temperature, and Φ is electrolyte potential. In Equation 2 the Nernst-Einstein relation has been utilized to relate the mobility to the diffusivity of species i. It should be noted that the *dilute* solution approximation is a reasonable one in the present work since the mole fractions of charged species (e.g. Ni^{2+}, SO_4^{2-}) of typical nickel plating baths are on the order of a few percent; for example, a 330 *g/L* Watts nickel bath with a nickel content of 330 *g/L* yields a mole fraction of 0.0219 for Ni^{2+}.

2.2 Electrolyte potential

Multiplying Equation 1 by z_iF, summing over all n species, applying the assumption of electroneutrality ($\sum c_i z_i = 0$), and then substituting Equation 2 into the resultant equation, we obtain an equation that explicitly describes the electrolyte potential:

$$\nabla \cdot (\mathbf{i}_m + \mathbf{i}_d) = F \sum_{i=1}^{n-1} z_i r_i \qquad (3)$$

where

$$\mathbf{i}_m = -\kappa \nabla \Phi = -\left[\sum_{i=1}^{n-1} \frac{F^2}{RT} z_i^{\,2} D_i c_i \right] \nabla \Phi \qquad (4)$$

and

$$\mathbf{i}_d = -F \sum_{i=1}^{n-1} z_i D_i \nabla c_i \qquad (5).$$

In Equations 3 – 5, the summation runs from 1 to n-1 because water has been designated as the n^{th} species and has a charge number of zero (electroneutrality). In Equation 3 $\mathbf{i}_m$ is the current density vector due to migration of charged species driven by the electrolyte-potential gradient whereas $\mathbf{i}_d$ is the current density vector due to diffusion of charged species driven by their concentration gradients.

2.3 Velocity and hydrodynamic pressure

For electrodeposition involving *dilute* aqueous electrolyte solutions and bath stirring, the electrolyte solutions can be safely taken as Newtonian liquids; consequently, the velocity field, **u**, is described by the following equations of momentum conservation (cf. Schunk et al. 1997, Newman 1991, and Bird et al. 2002) when buoyancy-induced natural convection can be neglected (Equation 6 is essentially the Navier-Stokes equation in slightly unfamiliar form for flow involving a moving boundary):

$$\rho \frac{d\mathbf{u}}{dt} + \rho(\mathbf{u} - \mathbf{u}_m) \cdot \nabla \mathbf{u} = -\nabla p + \rho \mathbf{g} + \mu \nabla^2 \mathbf{u}, \qquad (6)$$

where ρ and μ are, respectively, density and viscosity of electrolyte solution, p is hydrodynamic pressure, and $\boldsymbol{g}$ is the gravitational body force vector. In our case studies in which effects of buoyancy-induced natural convection can be neglected, ρ is taken to be constant. Consequently, the continuity equation of the mixture or electrolyte solution is given by:

$$\nabla \cdot \mathbf{u} = 0 \qquad (7).$$

Equation 7 is used to determine the hydrodynamic pressure field in the fully coupled system of governing equations.

To study the effects of buoyant convection on deposition of a metal such as nickel, we describe the variation of electrolyte-solution density, ρ (due to concentration variation of depositing-metal ion, e.g. Ni^{2+}) using the well-known Boussineq approximation (cf. Gebhart et al. 1988):

$$(\rho - \rho_{ref})\mathbf{g} \approx \rho_{ref} \mathbf{g} \beta^* (c_{Ni^{2+}} - c_{Ni^{2+},ref}) \qquad (8)$$

where $\beta^* = -(1/\rho_{ref})/(\partial \rho / \partial c_{Ni^{2+}})$, $c_{Ni^{2+}}$ is the molar concentration of Ni^{2+} ions, and subscript *ref* denotes some reference state. In Equation 8, a derivative with respect to the concentration of SO_4^{2-} is not included because the density of an electrolyte solution of $NiSO_4$ can be written in terms of the concentration of just one of the species (due to electroneutrality). In order to obtain $\partial \rho / \partial c_{Ni^{2+}}$ needed for estimating β^*, the density of an aqueous solution of nickel sulfate is taken as (cf. Dean 1973):

$$\rho = 0.99952 + 8.6502 x_{Ni^{2+}} \qquad (9)$$

where ρ is in units of g/cm^3. Lastly, to account for buoyancy effects, the momentum equation is accordingly modified as follows:

$$\rho \frac{d\mathbf{u}}{dt} + \rho(\mathbf{u} - \mathbf{u}_m) \cdot \nabla \mathbf{u} = -\nabla p + (\rho - \rho_{ref})\mathbf{g} + \mu \nabla^2 \mathbf{u} \qquad (10).$$

2.4 Pseudo-solid mesh nodal displacement

To solve for the nodal displacements of the finite-element mesh (employed in numerically solving the equations that govern the physical phenomena involved), we employ an arbitrary-Lagrangian-Eulerian formulation as developed by Sackinger et al. (1995) and treat the mesh as a pseudo solid that obeys the following equilibrium stress equation (Sackinger et al. 1995, and Schunk et al. 1997):

$$\nabla \cdot \mathbf{T} = 0 \qquad (11)$$

where

$$\mathbf{T} = 2\mu_m \mathbf{E} + \lambda_m tr(\mathbf{E})\mathbf{I} \tag{12}$$

and

$$\mathbf{E} = \frac{1}{2}\left[(\nabla \mathbf{d}) + (\nabla \mathbf{d})^T\right] \tag{13}.$$

In the above equations **d** is the mesh displacement vector, **I** is the identity matrix, and μ_m and λ_m are the Lame elastic coefficients, which are related to the familiar Young's modulus and Poisson ratio of the pseudo solid.

2.5 Rate of metal-ion reduction via Butler-Volmer kinetics

The rate of reduction reaction for metal-ion species *i* is taken to be described by the Butler-Volmer kinetics (cf. Newman 1991, Pollard and Newman 1981):

$$r_i = k_i c_i^{\beta_i}\left[e^{\alpha_{a,i}\frac{F}{RT}(V-\Phi-U_{0,i})} - e^{-\alpha_{c,i}\frac{F}{RT}(V-\Phi-U_{0,i})}\right] \tag{14},$$

where k_i, β_i, $\alpha_{a,i}$, and $\alpha_{c,i}$ are, respectively, the rate constant, reaction order, anodic transfer coefficient and cathodic transfer coefficient of metal-ion species *i*; $U_{0,i}$ is the thermodynamic open-circuit potential of the reduction reaction involving metal-ion species *i*. *V* is the external voltage applied to the cathode (i.e., deposition surface).

2.6 Electrical current density on deposition surface

Using Faraday's law the electrical current density normal to the deposition surface can be computed as follows:

$$\mathbf{n}\cdot\mathbf{i} = \mathbf{n}\cdot\left(\sum_{i=1}^{m}\mathbf{i}_i\right) = \sum_{i=1}^{m} z_i F r_i \tag{15}$$

where $\mathbf{i}$ is the total current density whereas $\mathbf{i}_i$ denotes the partial current density for metal-ion species *i*, **n** is a unit vector normal to the deposition surface, and *m* is the total number of reducible metal ions present in the electrolyte solution.

2.7 Position of the moving deposition surface

The position of the moving deposition surface is determined by local mass balances on the metal being deposited at the surface. For pure nickel metal deposition, which is the focus of the present work, local mass balance on the nickel at the surface yields:

$$\frac{dh}{dt} = \mathbf{n} \cdot (\mathbf{u}_s - \mathbf{u}_m) = \frac{M_{Ni}}{\rho_{Ni}} r_{Ni} \tag{16}$$

where h is the displacement or movement normal to the moving deposition surface relative to a mesh moving with local velocity $\mathbf{u}_m$, $\mathbf{n}$ is unit vector normal to the deposition surface, and $\mathbf{u}_s$ is velocity of the deposition surface; ρ_{Ni} is the density of the nickel deposit, M_{Ni} is the molecular weight of the nickel deposit, and r_{Ni} is the molar rate of Ni^{2+} reduction as given by Equation 14.

2.8 Theoretical or maximum thickness of deposition

The theoretical or maximum thickness of nickel deposition can be obtained from Faraday's law under the supposition of a current efficiency of 100%:

$$h_0 = \frac{M_{Ni} i_{ave} t}{\rho_{Ni} z_{Ni^{2+}} F} = \frac{M_{Ni}}{\rho_{Ni}} \frac{i_{ave} t}{2F} \tag{17}$$

where h_0 denotes the theoretical or maximum deposition thickness; i_{ave} is average applied current density; t is deposition time; and $z_{Ni^{2+}}$ is the charge number for Ni^{2+} ions ($z_{Ni^{2+}} \equiv 2$). Using $M_{Ni} = 58.71$ *g/mole*, $\rho_{Ni} = 8.9$ *g/cm*^{3}, and we obtain a simple equation for the maximum achievable thickness of nickel deposition:

$$h_0 = 3.42\text{x}10^{-5} i_{ave} t \tag{18}.$$

In Equation 18 h_0 is in units of *cm*; i_{ave} is in units of *A/cm*^{2}; and t is in units of *seconds*. It is informative to find from Equation 18 the theoretical or minimum time needed to deposit 1 *mm* thick nickel metal. Using an average current density of 50 *mA/cm*^{2}, it takes a minimum of 16.2 *hours* to achieve a 1 mm thick nickel deposit. Of course, it takes longer in practice since electrode efficiencies are less than 100% and transport resistance is significant, particularly for deposition in deep trenches.

2.9 Asymptotic thickness of deposition in the dominating migration flux regime

When migration flux dominates over diffusion flux (as is the case when deposition operates at sufficiently high current densities and species concentration gradient is small), the flux for Ni^{2+} can be obtained from Equation 2 by dropping the diffusive-flux term:

$$\mathbf{J}_{Ni^{2+}} \approx -\frac{F}{RT} z_{Ni^{2+}} D_{Ni^{2+}} c_{Ni^{2+}} \nabla\Phi = -\frac{2FD_{Ni^{2+}} c_{Ni^{2+}}}{RT} \nabla\Phi \tag{19}.$$

From Equation 4, we have:

$$\nabla\Phi = -\frac{i_m}{\kappa} \approx -\frac{i_{ave}}{\kappa} \tag{20}$$

where

$$\kappa = \sum_{i=1}^{2} \frac{F^2}{RT} z_i^{\,2} D_i c_i = \frac{F^2}{RT} (z_1^{\,2} D_1 c_1 + z_2^{\,2} D_2 c_2) = \frac{4F^2}{RT} (D_{Ni^{2+}} c_{Ni^{2+}} + D_{SO_4^{2-}} c_{SO_4^{2-}}) \tag{21}.$$

Substituting Equation 21 into Equation 20 and then into Equation 19 yields:

$$J_{Ni^{2+}} \approx \frac{i_{ave} D_{Ni^{2+}} c_{Ni^{2+}}}{2F(D_{Ni^{2+}} c_{Ni^{2+}} + D_{SO_4{}^{2-}} c_{SO_4{}^{2-}})} \tag{22}.$$

Now, electroneutrality ($\sum c_i z_i = 0$) demands that $c_{Ni^{2+}} = c_{SO_4{}^{2-}}$, consequently Equation 22 reduces to:

$$J_{Ni^{2+}} \approx \frac{i_{ave} D_{Ni^{2+}}}{2F(D_{Ni^{2+}} + D_{SO_4{}^{2-}})} \tag{23}.$$

Using the fact that one mole Ni^{2+} ions produces one mole of Ni, assuming that $J_{Ni^{2+}}$ remains constant during the course of deposition, and making use of Faraday's law, we arrive at an approximate expression for the nickel deposition thickness in the regime of dominating migration flux:

$$h_1 \approx \frac{M_{Ni}}{\rho_{Ni}} \frac{i_{ave} t}{2F} \frac{D_{Ni^{2+}}}{(D_{Ni^{2+}} + D_{SO_4{}^{2-}})} \tag{24}.$$

2.10 Numerical solution method, re-meshing and re-mapping

The governing equations (1) – (5), (6) – (7) or (8) – (10), and (11) – (14) are solved in GOMA, using i) finite-element discretization with structured/unstructured meshes generated by CUBIT (see [4]); ii) Galerkin weighted residuals with quadratic basis function for species concentrations, electrolyte potential, velocity, pressure, and nodal displacement unknowns; iii) a fully-coupled implicit solution scheme via Newton's method; adaptive time-step control (Adams-Bashforth predictor, Moulton corrector); and parallel computing employing an iterative solver for the solution of the resultant $\mathbf{Ax} = \mathbf{b}$ matrix-vector equations. Further details on the numerical solution method can be found in the GOMA user's guide (Schunk et al. 1997, Schunk et al. 2002). Results presented in this paper were all computed on a 48-processor network of 400 MHz Sun Workstations using eight processors.

To handle the dramatic reduction in the depth of trench-like electrolyte domain(s) and to avoid mesh distortion, we perform re-meshing every 10 – 20 time steps (depending on process conditions and whether or not the deposition surface is approaching the top of the trench) using CUBIT. Solution variables were mapped from the old mesh to the new mesh using MAPVAR. We automated the process of re-meshing and re-mapping using a Unix script.

3. Computational Results and Discussion

3.1 Model geometry and electrolyte system

Figure 5 shows the single-trench model geometry used in our studies, which consists of a 1*cm* x 1*cm* square electrolyte bath and a 1*mm* x 1*mm* square trench. Figure 6 displays the two-trench model geometry, which consists of a 1*cm* x 2*cm* rectangular electrolyte bath, a

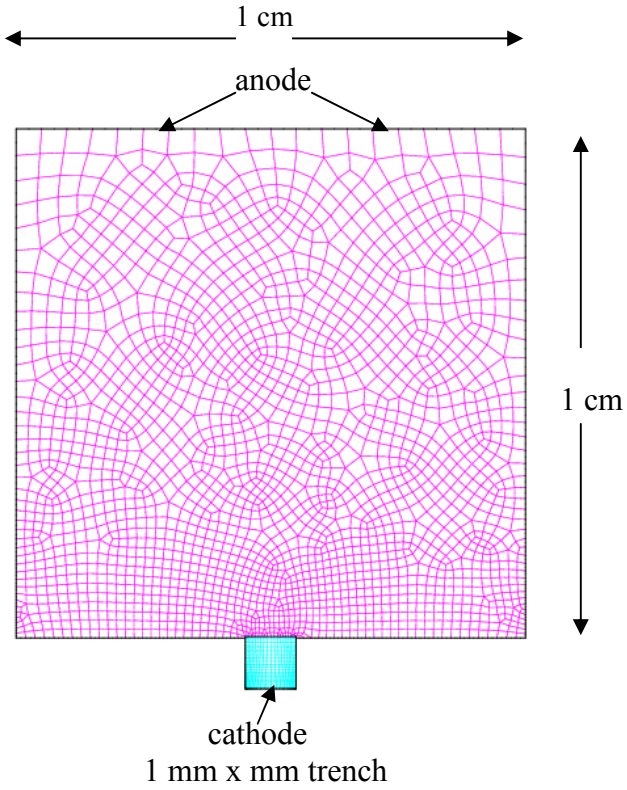

Figure 5. Model geometry of LIGA electrodeposition in a single trench – initial finite element mesh employed in the case study simulations.

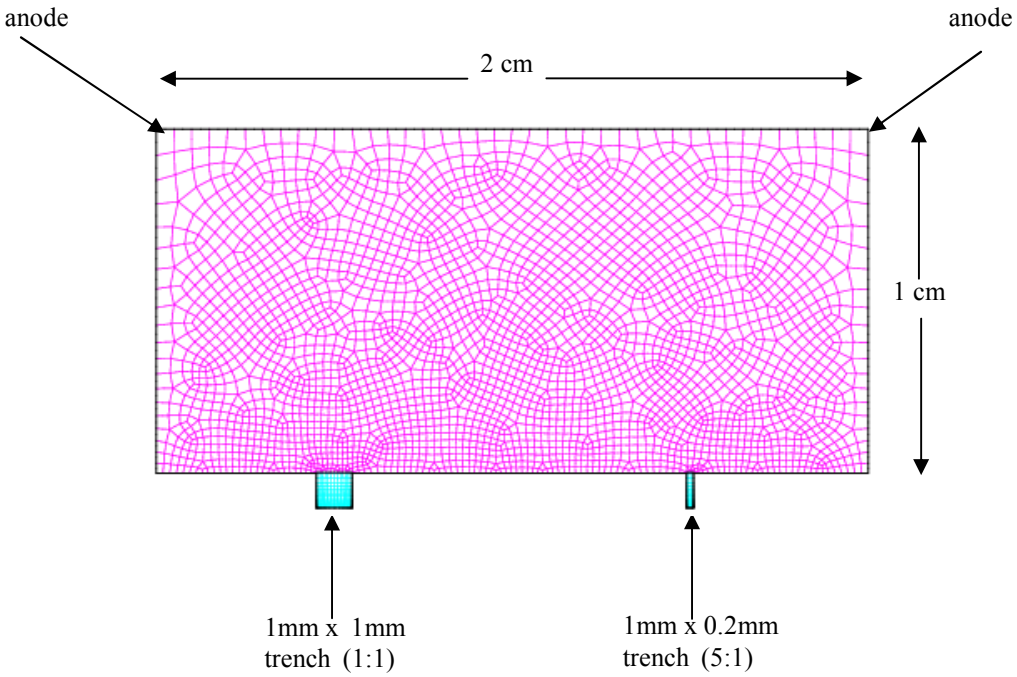

Figure 6. Model geometry of LIGA electrodeposition in two trenches – initial finite element mesh employed in the case study simulations.

1 *mm* x 1*mm* square trench and a 1 *mm* x 0.2 *mm* rectangular trench. Also displayed in Figures 5 and 6 are the initial finite-element meshes that were employed in the respective case-study simulations. Mesh refinement studies were carried out to arrive at these unstructured and sufficiently fine meshes. The two-trench mesh shown in Figure 6 has *3167* elements, which results in a total of *41,151* unknowns. This modest number of unknowns is the result of a strategy aimed at reducing computational cost: the mesh structure in the bath domain is considered fixed so that the mesh-motion equations are solved only in the trench domains; otherwise, the total number of unknowns would have been much higher. For simplicity, a model electrolyte system consisting of Ni^{2+}, SO_4^{2-} and H_2O was selected. This model electrolyte system corresponds to a Watts nickel electroplating bath in the absence of additives. Also for simplicity, the homogeneous dissociation reactions are taken to be infinitely fast and the bath pH is assumed to be maintained below 4 such that the concentration of $Ni(OH)^+$ is more than five orders of magnitude smaller than the concentrations of Ni^{2+}, SO_4^{2-} and H_2O, and that $Ni(OH)_2$ precipitation does not occur – this is clearly shown in the species-concentrations vs. pH diagram presented in the Appendix.

3.2 Boundary conditions

The nickel-metal anode is taken to cover the entire top surface of the bath. Along the anode surface, molar concentrations of Ni^{2+} and SO_4^{2-} are fixed at their initial values, and the electrolyte potential is set to zero in order to establish its datum. Along the side walls of the bath and the trenches and on the bottom surface of the bath, zero flux conditions are applied for the species-mass and charge conservation equations. Along the moving cathodic deposition surface(s) at the bottom(s) of the trench(es), the following conditions are imposed: 1) the total flux for the Ni^{2+} species is set to be equal to the rate of Ni^{2+} reduction as given by Equation 14; 2) the total flux for the SO_4^{2-} species is set to zero since the deposition reduction reaction does not involve SO_4^{2-} ; 3) the current density normal to the deposition surface is given by Equation 15 (in the electrolyte system chosen for the present study, Ni^{2+} is the only metal ion that is reduced). As mentioned previously in Section 3.1, the bath domain is considered fixed and the mesh-motion equations are solved only in the trench domain(s) in order to reduce computational cost. Boundary conditions for the mesh motion equations solved in the trenches are: a) the x-coordinates along the left and right side walls are fixed whereas the y-coordinates are not fixed along these boundaries; b) the y-coordinates along the top boundary (or boundaries) of the trench domain(s) are fixed whereas the x-coordinates are not fixed; c) along the moving deposition surface(s), the velocity normal to the deposition surface(s) is obtained from Equation 16. To locate the y-coordinates of the deposition surface(s) at sidewalls, the apparent angles of contact between the trench side walls and the deposition surface(s) at the contact lines are specified. Lastly, for constant total current operations (in which the total electric current to all deposition surfaces is fixed during electrodeposition), the total current is first computed by assuming a cathode voltage and integrating the local current density over the deposition surface for each trench and then summing up the current contribution from each trench. This computed total current is made equal to the total current specified by iterative adjustment of the cathode voltage common to all deposition

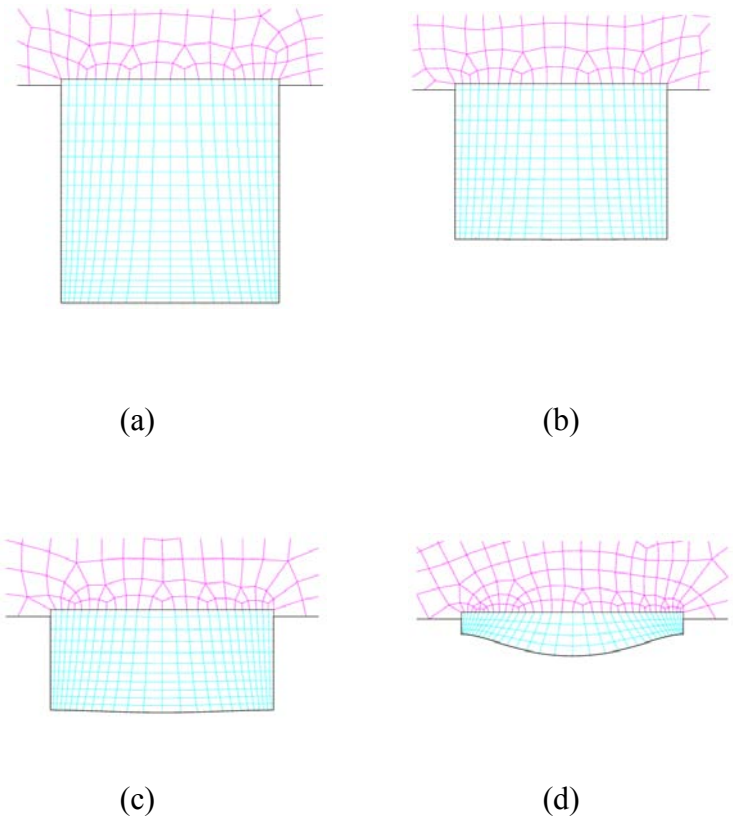

Figure 7. Mesh topology employed at four different deposition times
(a) 1 second; (b) 10 hours; (c) 19 hours; and (d) 29 hours.

surfaces. This iteration is accomplished by augmenting a total specified current constraint to the overall matrix system of equations.

3.3 An example of re-meshing

Figure 7 shows an example of re-meshing in the trench and its vicinity in the case of single-trench deposition. As clearly displayed in Figure 7, the trench height or depth shrinks as time increases and the number of rows of elements are accordingly reduced. Initially (at 1 second), 21 rows of elements were called for along the y-axis whereas only four rows of elements were needed toward the end of deposition (at 29 hours).

3.4 Goma electrodeposition model verification and validation

To verify that the GOMA electrodeposition model works properly, we first check if the electroneutrality constraint is satisfied. For the chosen electrolyte model system that consists of Ni^{2+}, SO_4^{2-}, and H_2O, electroneutrality requires that the concentrations of Ni^{2+} (species 1) and SO_4^{2-}(species 2) be equal. Figure 8 shows the species concentration profiles (from the top bath surface to the deposition surface) computed by GOMA for one-dimensional electrodeposition after 25 hours of deposition. Clearly from Figure 8, the electroneutrality constraint is completely satisfied since the concentrations of Ni^{2+} (species 1) and SO_4^{2-}(species 2) are identical from the top bath surface to the deposition

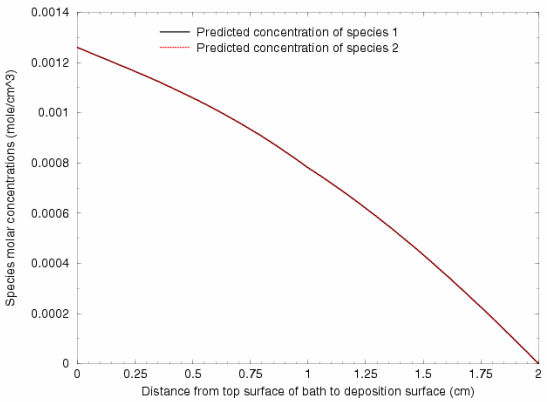

Fig. 8. Species concentration profiles from top bath surface to deposition surface as computed by GOMA in 1-D deposition (at deposition time = 25 hours)

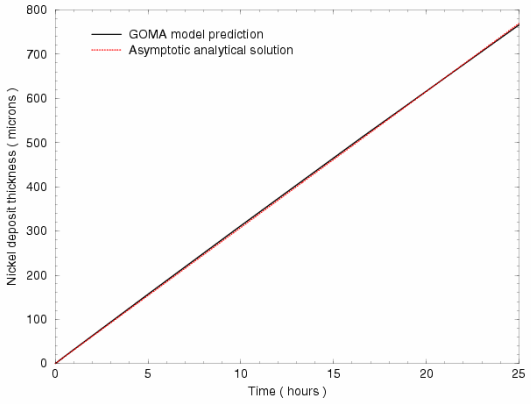

Fig. 9. Comparison between analytical solution and GOMA prediction in the asymptotic regime of dominating migration flux

Parameters (for cases in Figures 8 & 9): average curren density = 50 mA/cm^2, $D_1 = D_2 = 0.5\text{x}10^{-5}$ cm^2/s, k_1 = 0.0005 cm/s, $\beta_1 = 1$, $\alpha_a = \alpha_c = 0.21$, $U_{0,1}$ = -0.22 volt, $c_1^0 = c_2^0 = 0.00126$ moles/cm^3, $T = 40\ ^oC$.

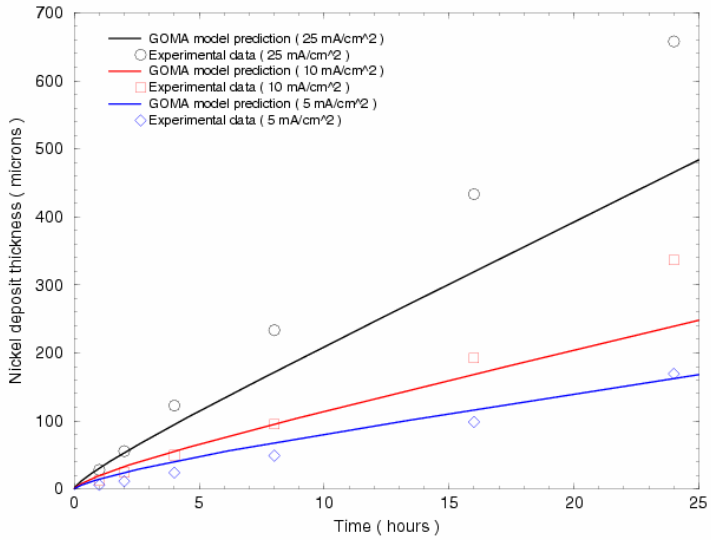

Figure 10. Deposition thickness computed by GOMA vs. Experimental data

surface (the difference, if any, is indiscernible). Next, we computed the thickness of one-dimensional deposition using GOMA and analytically (Equation 24) in the asymptotic regime of dominating migration flux and constant electrolyte conductivity and the results are presented in Figure 9. For the 25 hours of deposition time studied, the agreement between the analytically computed thickness and GOMA prediction is excellent. Lastly, Figure 10 compares the deposition thickness as computed by GOMA with the experimental data obtained by Prof. B. N. Popov of the University of South Carolina (Popov 2002) under three different deposition current densities: 5, 10, 25 mA/cm^2. Reasonably good agreement is achieved for the case of low current density (5 mA/cm^2). Discrepancy arises as deposition current density increases – this is most likely due to that forced and buoyant flows were not accounted for in the GOMA prediction.

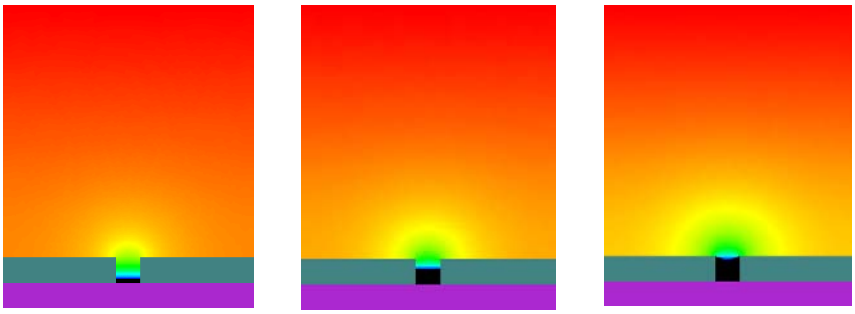

(a) (b) (c)

Figure 11. Computed contours of electrolyte potential & position of deposition surface in nickel deposition with a single trench: (a) 5 hours; (c) 20 hours; (c) 30 hours.

3.5 Electrodeposition in absence of bath stirring

Nickel deposition in a single trench. Figure 11 shows the computed electrolyte potential and position of the moving deposition surface in nickel deposition with a single trench in the absence of bath stirring at three different times: 5, 20, and 30 hours (when the trench is filled). The parameters used in the computations are (subscripts 1 and 2 denote Ni^{2+} and SO_4^{2-}, respectively): $\mu_m = 1$, $\lambda_m = 0.1$, $D_1 = D_2 = 10^{-5}$ cm^2/s, $k_1 = 0.0001$ cm/s, $\beta_1 = 1$, $\alpha_a = \alpha_c = 0.21$, $V = -0.6$ volt, $U_{0,1} = -0.22$ volt, $c_1^0 = c_2^0 = 0.00126$ moles/cm^3, $T = 40$ ^{o}C, θ_c (contact angle at side walls) = 90^o. Since the cathode (i.e., deposit) potential is fixed at -0.6 volt so this is a constant voltage operation. In Figure 11, colors in the bath and trench regions indicate electrolyte potential levels with red (top of the bath) denoting the datum (i.e., $\Phi = 0$) and light blue (deposition surface) referring to the most negative value of Φ. The black regions indicate the nickel deposit. As shown in Figure 11, electrolyte potential becomes increasingly more negative from the anode (top of bath) to the cathode (deposition surface), which creates a positive potential gradient for charge-species migration. Moreover, the deposition surface is essentially flat at early times of deposition but it then becomes increasingly curved as deposition approaches the top of the trench.

Figure 12a shows concentration profiles of Ni^{2+} (species 1) and SO_4^{2-} (species 2) at time = 20 hours whereas Figure 12b displays species concentrations at the center and side walls of the single trench of the deposition surface as a function of time. Parameters used here are the same as those in Figure 11. That the concentrations of species 1 and 2 are equal indicates that the electroneutrality constraint is perfectly met and that the governing equations are solved properly. As expected, the concentration of species 1 (Ni^{2+}) decreases from the anode surface to the cathodic deposition surface due to the reduction reaction in which Ni^{2+} is consumed.

Figure 13 shows the computed Ni^{2+} current density on the single-trench deposition surface (at the center and side walls) as a function of time. Parameters used here are the same as those in Figure 11. As can be seen clearly, current density is fairly uniform along deposition surface for the first 14 hours or so of electrodeposition (the trench is about 40% filled at this point). As the trench is filled to beyond 40%, the current density at the center of the deposition surface decreases whereas it increases at side walls. It is expected that microstructure (e.g., grain size) of nickel deposit will vary from the center to the side

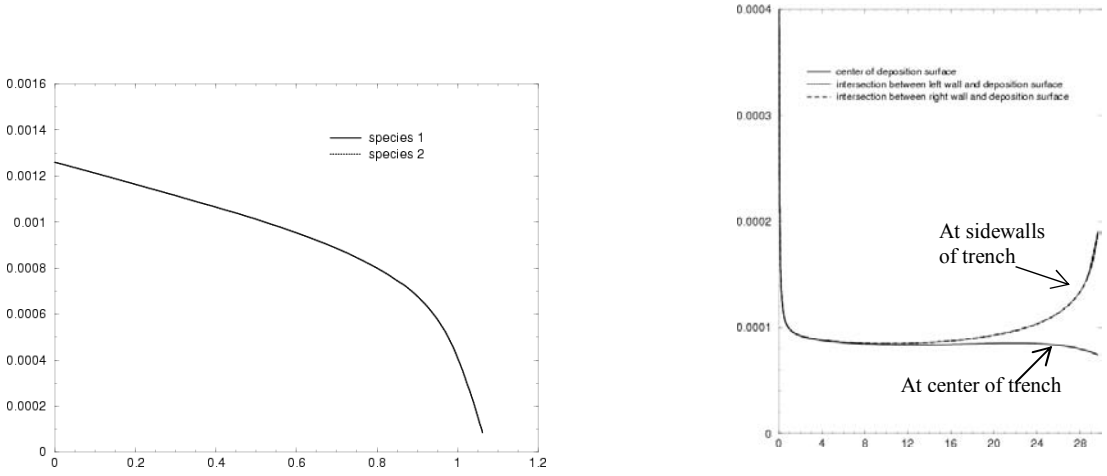

(a) (b)

Figure 12. Computed species concentrations (single trench): (a) concentrations along bath and trench centerline at 20 hours; (b) concentration as a function of time at deposition surface. Parameters here are the same as those in Figure 11.

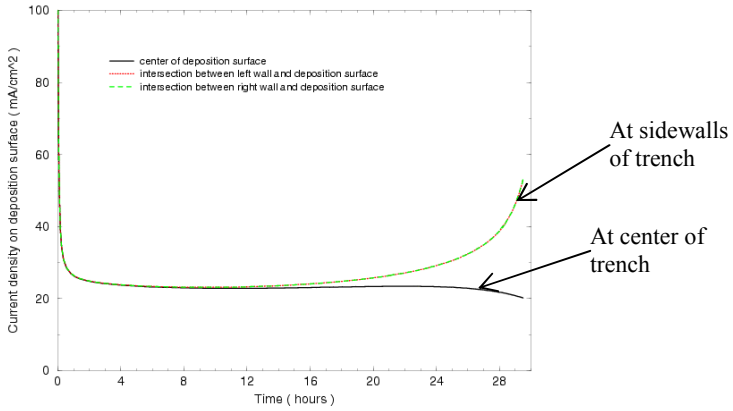

Figure 13. Computed Ni^{2+} current density on deposition surface vs. time (single trench).

walls of the trench due to variation in current density. Though at present constitutive models are still lacking to relate deposit grain size to current density, particularly to the current density at the deposition surface, it is well known that grain size is strongly dependent on the alloy composition which in turn, depends upon the current density. As shown in Figure 14, the yield stress of nickel deposit inversely varies with deposit grain size – the smaller the grain size, the higher the yield stress. In practice, nickel deposit grain size can be reduced by the use of grain-refinement additives such as saccharin and pulse plating (e.g., Goods et al. 2003).

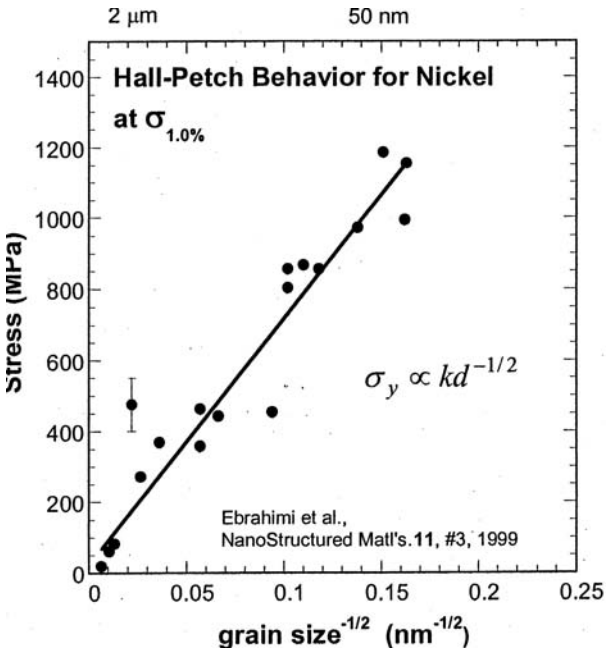

Figure 14. Yield stress as a function of nickel grain size
(Ebrabimi et al. 1999, courtesy of Steve Goods (8754))

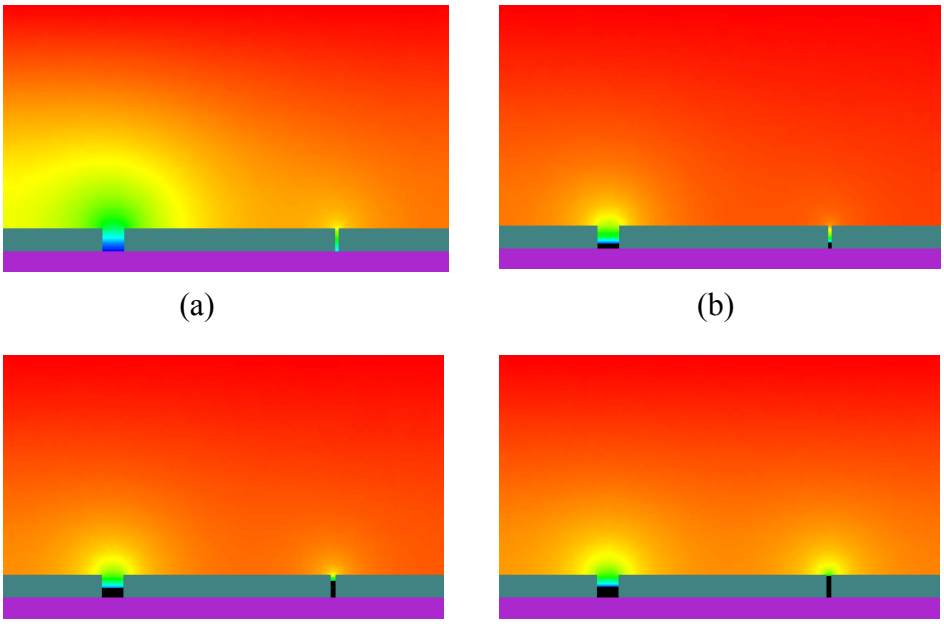

(a) (b)

(c) (d)

Figure 15. Computed contours of electrolyte potential and position of deposition surfaces (two trenches).

(a) 1 second; (b) 5 hours; (c) 13 hours; (d) 16 hours.

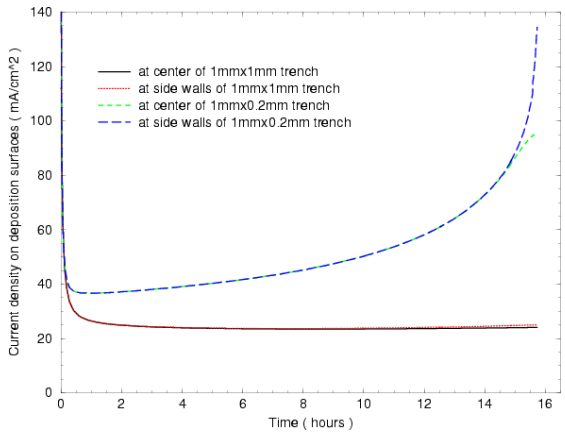

Fig. 16a. Computed Ni^{2+} current density at the deposition surfaces as a function of time for both trenches – constant voltage operation

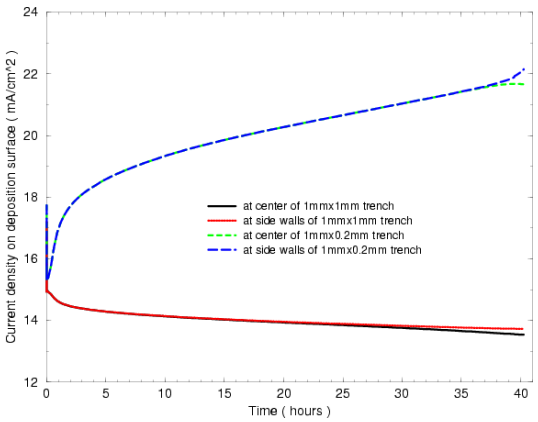

Fig. 16b. Computed Ni^{2+} current density at the deposition surfaces as a function of time – constant total current operation

Nickel deposition in two trenches. Figure 15 displays the electrolyte potential field and positions of deposition surfaces in nickel deposition with two trenches in the absence of bath stirring at four different times: at one second and at five, thirteen, and sixteen hours. Parameters used in the computation are the same as those for Figure 11, and similarly since the cathode (i.e., deposit) potential is fixed at -0.6 volt so this is a constant voltage operation. Colors in the bath and trench regions indicate electrolyte potential levels with red (top of the bath) denoting the datum (i.e., $\Phi = 0$) and light blue (deposition surface) referring to the most negative value of Φ. The black regions indicate the nickel deposit. The electrolyte potential becomes increasingly more negative from the anode (top of bath) to the cathodes (deposition surfaces), creating the potential gradients necessary for current flow. For the process conditions and trench geometry chosen, it takes about 16 *hours* for the narrow trench to fill (Figure 15.d) whereas it takes about 30 *hours* for the wide trench to be completely filled. Although not apparent in Figure 15, the deposition surfaces are essentially flat at early times of deposition but they then become increasingly curved as deposited material approaches the tops of the trenches.

In Figure 16a, computed Ni^{2+} current density at the center of the narrow trench (with a 5:1 height-to-width aspect ratio) is compared with that of the wide trench under constant voltage operation with process parameters being the same as those for Figure 11. Clearly, the current density for the narrow trench is consistently higher than that for the wide trench, and this difference is more evident as deposition proceeds and approaches the top of the trenches – this explains why the narrow trench needs only about 16 *hours* to fill whereas the wide trench requires about 30 *hours*. Due to the different current densities, the microstructure of the deposit in the narrow trench may differ from that in the wide trench, which may result in differences in the mechanical properties of the deposits formed, particularly near the tops of the trenches.

Figure 16b shows a case of constant total current operation in which the total current applied is held at 1.8 mA (which gives an average current density of 15 mA/cm^2). The parameters used in the computations are the same as those for Figure 16a except here k_1 = 0.0001 cm/s and the cathode or deposit potential varies to accommodate a constant total current of 1.8 mA, which is supplied to the deposition surfaces in both trenches.

3.6 Effects of bath stirring

The effects of bath stirring on nickel electrodeposition in the 1 *mm* x 1 *mm* wide trench are illuminated in Figure 17 (in which the computed velocity field within the trench and immediately outside at six different times is shown) and Figure 18 (in which the computed streamlines both within and outside the trench at four different times are shown). Along the anode surface, the horizontal and vertical velocity components are set to 2 *cm*/*s* and 0, respectively. The no-slip condition is imposed on the side walls of the bath and trench. Other parameters are the same as those in Figure 15, except that here k_1 = 0.0005 *cm*/*s* and a current density of 50 mA/cm^2 is imposed on the deposition. As can be seen in Figure 18, only one re-circulation loop is present at the start of deposition whereas two re-circulations are present when the trench is about 65% filled. Approximately 18 hours are required to completely fill the trench as compared with about 24 hours in the absence of bath stirring, resulting in a desirable 25% speed up in deposition time. However, bath stirring also results in an undesirable curved deposition surface (i.e., local non-uniformity) as can be seen from Figures 17.f and 18.d .

3.7 Effects of buoyancy-induced convection

Effects of buoyancy-induced convection on the deposition process was investigated and the computed results are displayed in Figures 19 and 20. To simplify our analysis, only the trench domain was considered and the boundary conditions imposed at the top of the trench surface were: 1) horizontal velocity component was set at 1 cm/s whereas the vertical velocity component was set to zero; 2) molar concentrations of Ni^{2+} and SO_4^{2-} were fixed at 0.00126 moles/cm^3. The other parameters were the same as those used for

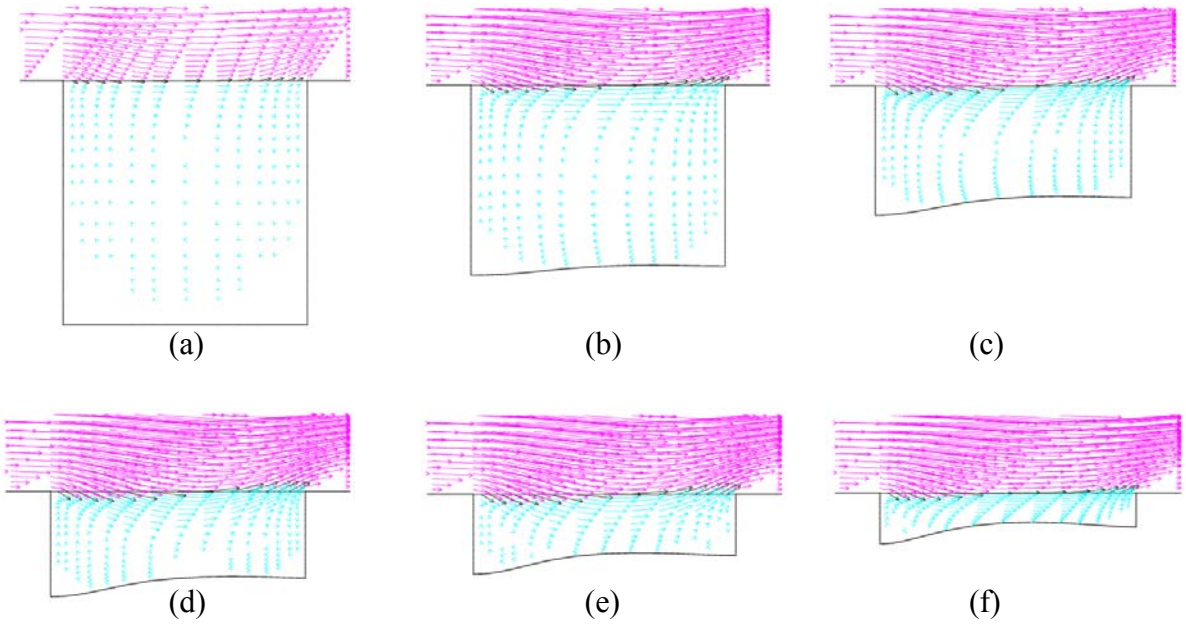

Figure 17. Effect of bath stirring on a single-trench deposition: velocity fields in the trench and its vicinity. (a) 1 second; (b) 5 hours; (c) 10 hours; (d) 12 hours; (e) 14 hours; and (f) 16 hours.

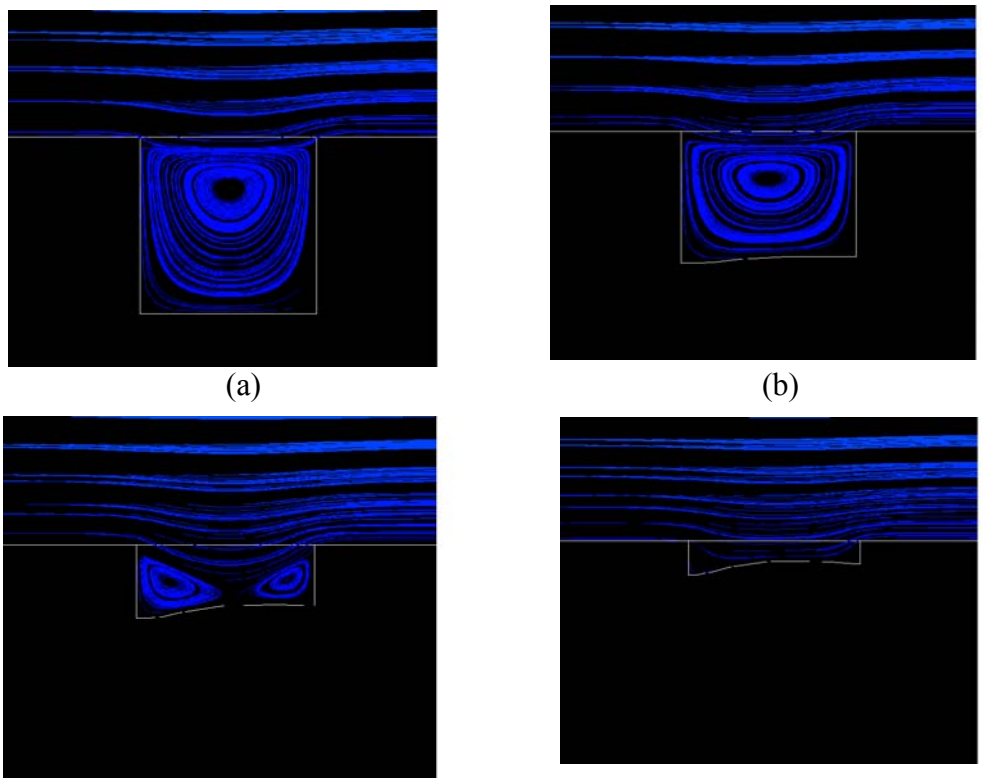

Figure 18. Effect of bath stirring on a single-trench deposition: streamlines in the trench and its vicinity. (a) 1 second; (b) 5 hours; (c) 12 hours; (d) 16 hours.

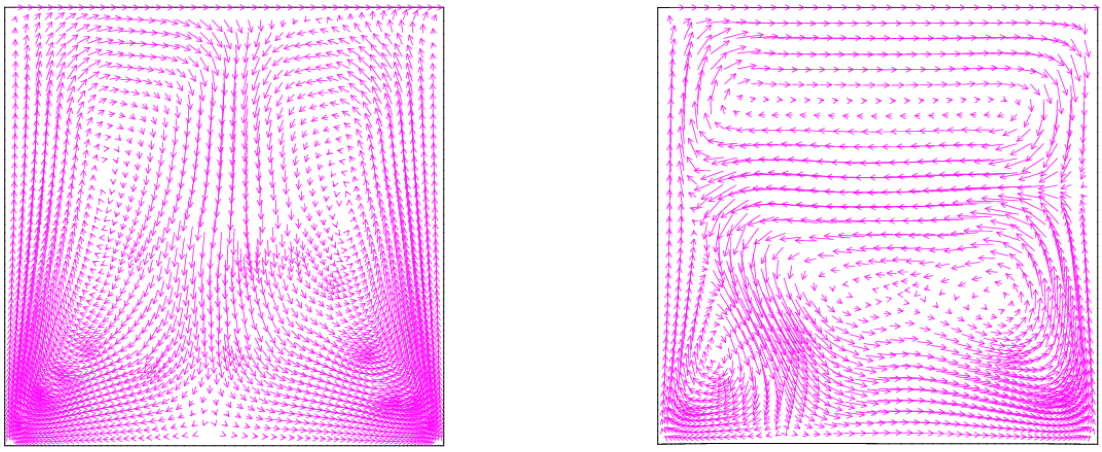

Figure 19. Effects of buoyancy on nickel electrodeposition: velocity vectors.
(a) t = 15 seconds; (b) t = 360 seconds.
Parameters: velocity at top surface – 0.01 m/s; 1 mm by 1 mm trench.
Other parameters are the same as those for Figure 11.

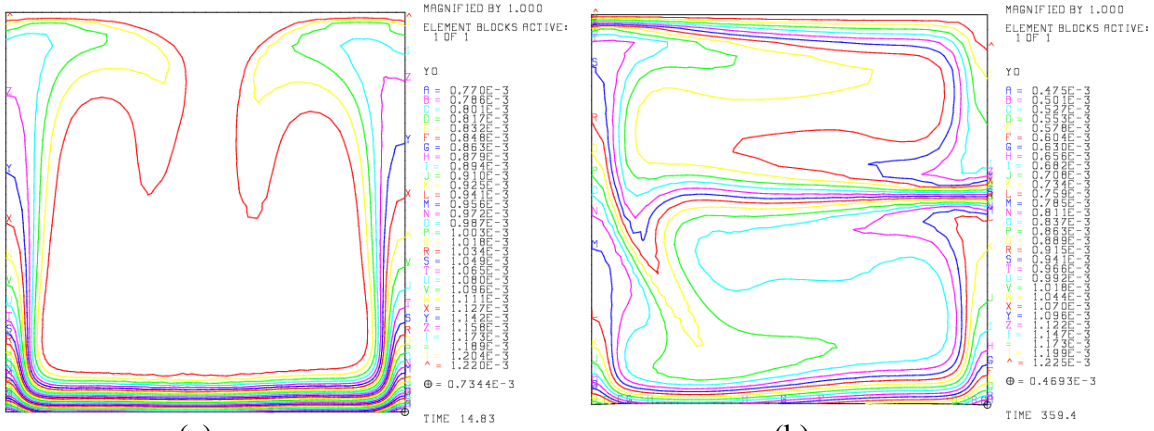

(a) (b)

Figure 20. Effects of buoyancy on nickel electrodeposition: Ni^{2+} ions concentration contours. (a) t = 15 seconds; (b) t = 360 seconds.
Parameters: velocity at top surface – 0.01 m/s; 1 mm by 1 mm trench.
Other parameters are the same as those for Figure 11.

Figure 11. Figures 19 and 20 show, respectively, the velocity vectors and Ni^{2+} ion concentration at two different times: 15 seconds and 360 seconds. From Figure 19, it is seen that fresh electrolyte solution is drawn from the center of the top surface and moves toward the bottom deposition surface whereas spent electrolyte solution rises upward near the side walls. Six minutes later, flow structure in the trench has changed significantly: two horizontal circulation cells have formed at 360 seconds as compared with one vertical cell at 15 seconds. A separate study in which longer deposition (up to 1650 seconds) was simulated though the horizontal velocity component imposed at the top surface was smaller (0.01 cm/s) was carried out and the results are documented elsewhere (Evans et al. 2002). In both studies, numerical instability in the form of wiggles at the deposition surface near the contact lines were observed when velocity at the top surface was raised or simulated deposition time was increased. Gradual mesh refinement did help alleviate the wiggle problem to a certain extent but eventually wiggles would appear at the deposition surface near the contact lines when sufficiently large velocity was imposed at the top surface of the trench or when long enough simulated deposition was carried out. Subsequent discussions with Prof. Thomas Hughes (who is an internationally renowned authority in computational mechanics and currently a professor of Aerospace and Engineering Mechanics at UT Austin) on this issue reveal that a variational multiscale formulation is required to resolve at a fine scale the wiggles (or numerical instabilities) appearing on the deposition surface though such studies await future efforts.

3.8 Electrodeposition in a microcreen-based LIGA mold

A novel process that enables the rapid and economical replication of plastic electroforming molds was developed recently by Domeier et al. (2002) at Sandia

National Laboratories. This process employs the hot embossing or the injection molding technique to force a metal microscreen into a softened thermoplastic disk to produce sacrificial electroforming molds with conducting metal bases and insulating sidewalls. Figure 21 shows a schematic of mold replication by hot embossing through a microscreen (Domeier et al. 2002). Figures 23 and 24 show the simulated effects of mold geometry (in terms of elevation of the conducting microscreen metal relative to the insulating polymethylmethacrylate or PMMA plastic) on deposition uniformity in the absence of bath stirring. In both calculations the modeled portion of the mold has a plating substrate comprised of two 50 μm wide metal electrode sections separated by a 100 μm PMMA insulator. Thus, in view of the symmetry conditions applied on the model sidewalls, the results apply to the infinite array of 100 μm electrodes separated by 100 μm PMMA insulators. Other parameters used in the computation are: $\mu_m = 1$, $\lambda_m = 0.1$, $D_1 = D_2 = 10^{-5}$ cm^2/s, $k_1 = 0.000005$ cm/s, $\beta_i = 1$, $\alpha_a = \alpha_c = 0.21$, $I = 0.3$ mA, $U_{0,1} = -0.22$ $volt$, $c_1^0 = c_2^0 = 0.00126$ $moles/cm^3$ and $T = 40^o$ C. Here I is the total applied electric current; for $I = 0.3$ mA, an average current density of 15 mA/cm^2 (based on the microscreen metal areas) is applied to the deposition process. In Figure 23 the microscreen metal is elevated relative to the base PMMA whereas in Figure 24 the base PMMA is elevated relative to the microscreen metal. The computations indicate that dimples will be formed on the deposit surface when the microscreen metal is elevated relative to the base PMMA (Figure 23); this prediction is born out by experimental observation shown in Figure 22. On the other hand, the deposit surface is essentially flat when the base PMMA is elevated relative to the microscreen metal (Figure 24). Thus, mold geometry appears to have an important effect on the deposition uniformity, which in turn may affect microstructure and functional/mechanical properties of the deposit.

4 Summary and Conclusions

Two dimensional processes of nickel electrodeposition were simulated using a framework that is based on the finite-element method and a fully coupled implicit solution scheme via Newton's technique. By coupling an ALE (arbitrary-Lagrangian-Eulerian) pseudo-solid mesh-motion formulation with repeated re-meshing and re-mapping, the evolving deposition surfaces were tracked and current densities (or rates of deposition) along deposition surfaces were computed. The relatively large computed variations in current density may cause significant variations in the microstructure and functional/mechanical properties of the deposit. The effects of bath stirring were also investigated; it was found that bath stirring can effectively reduce deposition time but also results in curved deposition surface(s) (and thus locally non-uniform rates of deposition). The Effect of buoyancy-induced convection on nickel electrodeposition was examined. Our preliminary results show that buoyancy strongly affects flow-field structure, and incorporating buoyancy in our computation model results in a much more stiff and challenging numerical problem to solve. More specifically, the numerical instability encountered when buoyancy is incorporated may be resolved by employing a variational multiscale formulation but such investigation awaits future efforts. Lastly, deposition in microscreen-based LIGA molds was simulated and it was discovered: i) elevating microscreen metal relative to adjacent base PMMA results in a deposit with

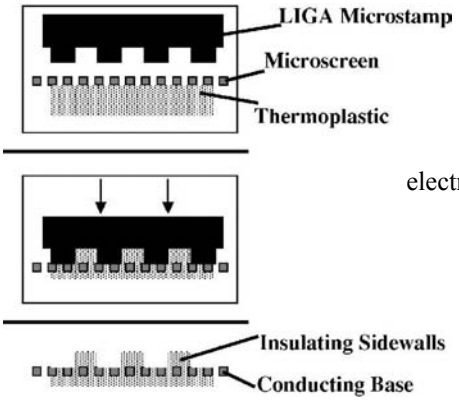

Fig. 21. Schematic of mold replication by hot embossing through a microscreen. (Reference: Domeier et al. 2002)

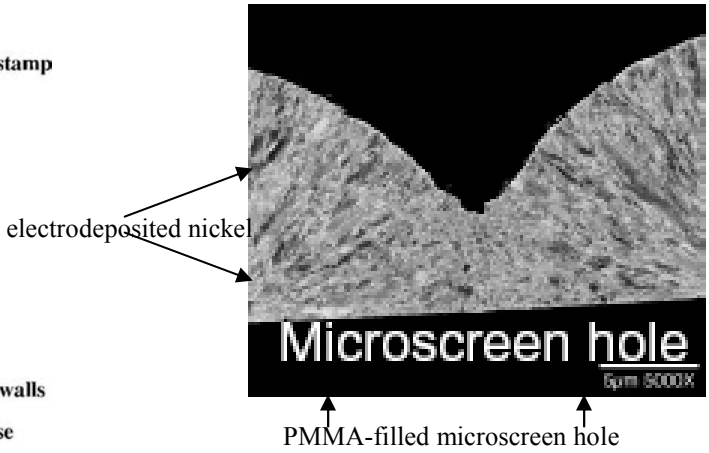

Fig. 22. Dimple deposit formed over a PMMA-filled microscreen hole. (Reference: Morales A. M. et al. 2003)

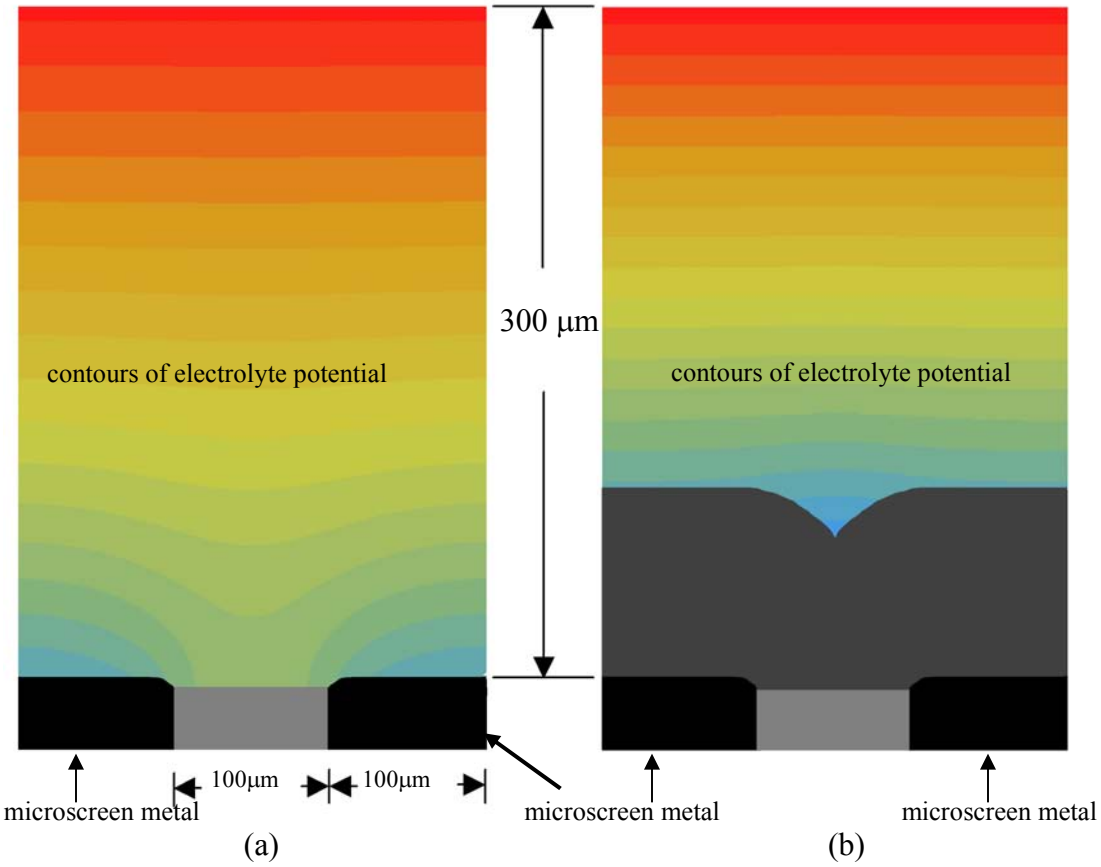

Figure 23. Electrodeposition in a microscreen-based LIGA mold — microscreen metal regions are elevated relative to insulating PMMA areas.
(a) at time = 0; (b) at time = 9.8 hours.

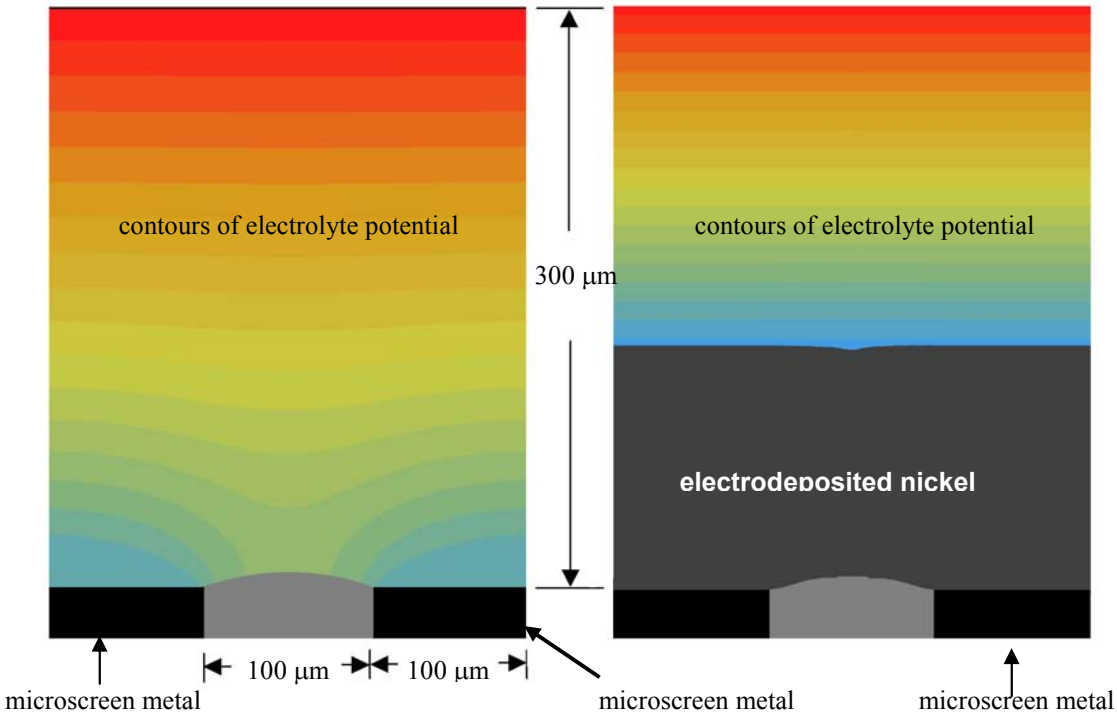

Figure 24. Electrodeposition in a microscreen-based LIGA mold — insulating PMMA regions are elevated relative to microscreen metal areas.
(a) at time = 0; (b) at time = 9.8 hours.

dimples, which is born out by experimental observation; and ii) elevating base PMMA relative to microscreen metal yields a nearly flat deposition surface, in which case the functional/mechanical properties may be essentially uniform.

The work reported here is part of a larger effort that aims at developing a model-based predictive computational capability at Sandia National Laboratories for simulating electrodeposition in LIGA microfabrication. Ongoing and future efforts include: 1) incorporating homogeneous (e.g., dissociation reactions, precipitation of $Ni(OH)_2^+$) and additional heterogeneous reactions (e.g., hydrogen generation) to study effects of electrolyte-solution pH and bath additives; 2) modeling alloy (e.g., Ni-Co) deposition; 3) determining effects of trench aspect ratio on current distribution; 4) studying effects of pulse plating on deposition dynamics and current distribution; 5) investigating effects of the use of insulating shields and location of anodes on current distribution; 6) developing models to relate deposit microstructure (e.g., grain size and orientation) to deposition current density; this will help us to better relate functional/mechanical properties of metal or alloy deposits to process conditions and bath chemistry; and 7) extending the application to the high aspect ratios (feature depth/width) of great importance to LIGA.

5 References

Bird, R. B., Stewart, W. E., and Lightfoot, E. N., *Transport Phenomena*, Second Edition, John Wiley & Sons, New York (2002).

Chen, K. S., "Modeling electrodeposition in LIGA microfabrication using an arbitrary-Lagrangian-Eulerian formulation for moving boundary tracking with repeated re-meshing", In Moving Boundaries VII: Computational Modeling of Free and Moving Boundary Problems, edited by Mammoli, A. A. and Brebbia, C. A., WIT Press Southampton, Boston, pp. 245 – 255 (2003).

Chen, K. S. and Evans, G. H., "Two-dimensional modeling of nickel electrodeposition in LIGA microfabrication", *Microsystem Technologies* (2004), in press.

Christenson, T., private communication (2000).

CUBIT, Version 8.0, Sandia National Laboratories (2003), URL: http://endo.sandia.gov/cubit .

Dean, J. A. (ed.), Lange's Handbook of Chemistry, 11th edition, McGraw-Hill, New York (1973).

Domeier, L. A., Gonzales, M., Hachman, J., Hruby, J. M., Janek, R., and Morales, A. M., "Microscreen-based replication of electroforming micromolds", *Microsystem Technologies*, **8**, p.78-82 (2002).

Evans, G. H., Chen, K. S., Larson, R. S., and Greif, R., "Forced and buoyancy-induced convection in LIGA electrodeposition", in Proceedings of the Twelfth International Heat Transfer Conference held in Grenoble, France, August 18 – 23, 2002. Edited by Jean Taine (2002).

Hruby, J. M., "LIGA technologies and applications", *MRS Bulletin*, April 2001.

Gebhart, B., Jaluria, Y., Mahajan, R. L., Sammakia, B., Buoyancy-Induced Flows and Transport, Textbook Edition, Hemisphere Publishing Corporation, New York, p.23 (1988).

Goods, S. H., Kelly, J. J., and Yang, N. Y. C., "Electrodeposited nickel-manganese: an alloy for microsystem applications", paper presented at the *Fifth International Workshop on High Aspect Ratio Micro Structure Technology, HARMST'03*, Monterey Plaza Hotel, Monterey, CA, June 15 – 17, 2003. Also to appear in *Microsystem Technologies*.

Griffiths, S. K., Nilson, R. H., Ting, A., Bradshaw, R. W., Bonivert, W. D., and Hruby, J. M., "Modeling electrodeposition for LIGA microdevice fabrication", *Microsystem Technologies*, **4**, pp. 98 - 101 (1998a).

Griffiths, S. K., Nilson, R. H., Bradshaw, R. W., Ting, A., Bonivert, W. D., Hachman, J. T., and Hruby, J. M., "Modeling electrodeposition for LIGA microdevice fabrication", *Sandia Technical Report* SAND98-8231 (1998b).

Hayashi, K., Fukui, K., Tanaka, Z., and Konko, K., "Shape evolution of electrodeposition bumps into deep cavities", *J. Electrochem. Soc.*, **148**, C145 – C148.

Morales, A. M., Domeier, L. A., Gonzales, M., Hachman, J., Hruby, J. M., Goods, S. H., McLean, D. E., Yang, N., Gardea, A. D., "Microstructure and mechanical properties of nickel microparts electroformed in replicated LIGA molds", *SPIE Proceedings*, **4979**: 440-447.

Newman, J. S., Electrochemical Systems, Second Edition, Prentice Hall, Inc., Englewood Cliffs, New Jersey (1991).

Nilson, R. H. and Griffiths, S. K., "Natural convection in trenches of high aspect ratio", *J. Electrochem. Soc.*, **150**, C401 – C412.

Polard, R. and Newman, J., "Mathematical modeling of the litium-aluminum, iron sulfide battery I. Galvanostatic discharge behavior", *J. Electrochem. Soc.*, **128**, 491 – 502.

Popov, B. N., "Electrodeposition of thin films of Ni in presence of organic additives", final report submitted to Sandia, April 2002.

Sackinger, P. A., Schunk, P. R., and Rao, R. R., A Newton-Raphson pseudo-solid domain mapping technique for free and moving boundary problems: a finite-element implementation, *J. Comp. Phys.*, **125**, p. 83-103 (1995).

Schunk, P. R., Sackinger, P. A., Rao, R. R., Chen, K. S., Cairncross, R. A., Baer, T. A., Labreche, D. A., "GOMA 2.0 - a full-Newton finite element program for free and moving boundary problems with coupled fluid/solid momentum, energy, mass, and chemical species transport: user's guide", *Sandia Technical Report* SAND97-2404 (1997).

Schunk, P. R., Sackinger, P. A., Rao, R. R., Chen, K. S., Baer, T. A., Labreche, D. A., Sun, A. C., Hopkins, M. M., Subia, S. R., Moffat, H. K., Secor, R. B., Roach, R. A., Wilkes, E. D., Noble, D. R., Hopkins, P. L., and Notz, P. K., "GOMA 4.0 - a full-Newton finite element program for free and moving boundary problems with coupled fluid/solid momentum, energy, mass, and chemical species transport: user's guide", *Sandia Tech. Report* SAND2002-3204 (2002).

Wellman, G. W., "MAPVAR – a computer program to transfer solution data between finite element meshes", *Sandia Technical Report* SAND97-0466 (1999).

6 Appendix – A Study of Solution Chemistry of Watts Nickel Plating Bath in Absence of Additives and Deposition Mechanism[¥]

Solution Chemistry: The solution chemistry of the Watts Nickel plating bath in absence of additives was studied by determining the equilibrium concentrations of the various species at different pH levels. The concentrations of all the electroactive species were determined by using various element balances, equilibrium conditions, and the electroneutrality condition at a specified pH. It was assumed that the bath consists of $NiSO_4$ and Na_2SO_4 dissolved in water. Suitable concentrations of H_2SO_4 or NaOH were used in the computation to obtain the concentration dependence as a function of pH. Sodium sulfate acts as a supporting electrolyte and helps in simplifying the mathematical computations. Nickel sulfate is the only source of nickel considered to simplify the number of species involved. The calculations had two parts - region I and region II. In region I, all electroactive species are completely dissolved. In region II, $Ni(OH)_2$ precipitates at higher pH levels. The governing equations for the various regions are as follows:

For region I, the variables to be determined are $[Ni^{2+}]$, $[Ni(OH)^{+}]$, $[OH^{-}]$, $[H_2O]$, $[SO_4^{2-}]$, $[HSO_4^{-}]$ and $[H_2SO_4]_{ad}$. The equations needed are

a) Element balance on Nickel

$$[Ni^{2+}]+[Ni(OH)^{+}]=[NiSO_4]_{ad} \qquad [1]$$

b) Element balance on Sulphur

$$[HSO_4^{-}]+[SO_4^{2-}]=[Na_2SO_4]_{ad}+[NiSO_4]_{ad}+[H_2SO_4]_{ad} \qquad [2]$$

c) Element balance on Oxygen

$$\begin{aligned}&[OH^{-}]+[Ni(OH)^{+}]+[H_2O]+4[HSO_4^{-}]+4[SO_4^{2-}]\\&=[H_2O]_{ad}+4[Na_2SO_4]_{ad}+4[NiSO_4]_{ad}+4[H_2SO_4]_{ad}\end{aligned} \qquad [3]$$

d) Electroneutrality condition

$$\begin{aligned}&[OH^{-}]+[HSO_4^{-}]+2[SO_4^{2-}]\\&=2[Na_2SO_4]_{ad}+[H^{+}]+2[Ni^{2+}]+[Ni(OH)^{+}]\end{aligned} \qquad [4]$$

e) Equilibrium relations

$$[H^{+}][SO_4^{2-}]-K_1[HSO_4^{-}]=0 \qquad [5]$$

$$[Ni^{2+}][OH^{-}]-K_2[Ni(OH)^{+}]=0 \qquad [6]$$

$$[H^{+}][OH^{-}]-K_3=0 \qquad [7]$$

[¥] Contribution from Prof. B. N. Popov (2002) as part of a final contract-project report to Sandia.

For region II, the variables to be determined are $[Ni^{2+}]$, $[Ni(OH)^{+}]$, $[Ni(OH)_2(s)]$,$[OH^{-}]$, $[H_2O]$, $[SO_4^{2-}]$, $[HSO_4^{-}]$ and $[NaOH]_{ad}$. The equations needed are

a) Element balance on Nickel

$$[Ni^{2+}]+[Ni(OH)^{+}]+[Ni(OH)_2(s)]=[NiSO_4]_{ad} \quad [8]$$

b) Element balance on Sulphur

$$[HSO_4^{-}]+[SO_4^{2-}]=[Na_2SO_4]_{ad}+[NiSO_4]_{ad} \quad [9]$$

c) Element balance on Oxygen

$$[OH^{-}]+[Ni(OH)^{+}]+[H_2O]+4[HSO_4^{-}]+4[SO_4^{2-}]+2[Ni(OH)_2(s)] = [H_2O]_{ad}+4[Na_2SO_4]_{ad}+4[NiSO_4]_{ad}+[NaOH]_{ad} \quad [10]$$

d) Electroneutrality condition

$$[OH^{-}]+[HSO_4^{-}]+2[SO_4^{2-}] = 2[Na_2SO_4]_{ad}+[H^{+}]+2[Ni^{2+}]+ [Ni(OH)^{+}]+[NaOH]_{ad} \quad [11]$$

e) In addition to the equilibrium conditions given above, we also have the relation

$$[Ni^{2+}][OH^{-}]^2-K_{d,Ni(OH)_2}=0 \quad [12]$$

The above set of equations were solved using Maple® with the use of appropriate values for the various constants.

Mechanism of Nickel Deposition: An adsorption model was developed in order to understand the mechanism of Ni deposition in sulfate electrolytes. In sulfate electrolyte, Ni^{2+} can be considered as the reactive species and the electrode kinetics is mainly governed by the competing reactions between hydrogen and nickel discharges. Nickel deposition involves the formation and subsequent reduction of intermediate adion (such as $NiOH_{ads}$), while the parasitic hydrogen evolution takes place through the formation of intermediate H_{ads}. For simplicity, the intermediate adsorbate of nickel is denoted as $(Ni^{+})_{ad}$. The mechanism of nickel deposition occurs via the reactions given below:

$$H^{+}+e^{-}\rightarrow H_{ads} \quad [13]$$

$$Ni^{2+}+e^{-}\rightarrow Ni^{+}_{ads} \quad [14]$$

$$Ni^{+}_{ads} + e^{-} \rightarrow Ni \quad [15]$$

$$Ni^{2+} + Ni^{+}_{ads} + 2e^{-} \rightarrow Ni + Ni^{+}_{ads} \quad [16]$$

$$Ni^{+}_{ads} + H^{+} + e^{-} \rightarrow Ni^{+}_{ads} + H_{ads} \quad [17]$$

$$2H_{ads} \rightarrow H_2 \quad [18]$$

$$Ni^{+}_{ads} + H_{ads} + 2e^{-} \rightarrow Ni + H_{incl} \quad [19]$$

According to these reactions, the adsorbed species Ni^{+}_{ads} is a precursor and a catalyst for the formation of the Ni deposit. However, this species also acts as a catalyst for hydrogen adsorption. Hence the surface coverages of these adsorbates will give an insight of the two cathodic processes occurring on the electrode surface. The material balance for the surface species are given by

$$\frac{d\theta_1}{dt} = A_{21}(1-\theta_1-\theta_2) - A_{22}\theta_1 \quad [20]$$

$$\frac{d\theta_2}{dt} = A_{20}(1-\theta_1-\theta_2) + A_{24}\theta_1 - A_{25}\theta_2^{\,2} - A_{26}\theta_1\theta_2 \quad [21]$$

where θ_1 and θ_2 are the electrode surface coverages of the two adsorbed species Ni^{+}_{ads} and H_{ads} respectively. Each reaction has a rate constant A_n (in mole cm^{-2} s^{-1}), which are defined according to the relation

$$A_n = a_n \exp(b_n(E-E_0)) \quad [22]$$

where b_n is the activation co-efficient, a_n includes both the rate constant and the concentration of the reacting species and E_0 is an arbitrarily chosen origin of potential to calculate the overpotential (set to zero in our simulations). With these formulations, the electron balances will yield the current relationship with the surface coverages. This relationship is given by the equation

$$i = F\beta(A_1(1-\theta_1-\theta_2) + A_2(1-\theta_1-\theta_2) + A_3\theta_1 + A_5\theta_1 + 2A_4\theta_1 \quad [23]$$

where F is the Faradaic constant and β is the maximum surface concentration on the electrode. In our work, simulations were performed using three different sets of parameters. The various sets of parameters are given below

Case 1 parameters

$$a_{20} = 1.2*10^{-7} cm^{-2}s^{-1}$$
$$a_{21} = 3.8*10^{-9} cm^{-2}s^{-1}$$
$$a_{22} = 1.52*10^{-8} cm^{-2}s^{-1}$$
$$a_{23} = 4*10^{-7} cm^{-2}s^{-1}$$
$$a_{24} = 1.08*10^{-9} cm^{-2}s^{-1}$$
$$a_{25} = 2*10^{-11} cm^{-2}s^{-1}$$
$$a_{26} = 1.56*10^{-9} cm^{-2}s^{-1}$$
$$b_{20} = b_{22} = b_{23} = b_{24} = b_{26} = 16V^{-1}$$
$$b_{21} = 30V^{-1}$$

Case 2 parameters

$$a_{20} = 1.2*10^{-6} cm^{-2}s^{-1}$$
$$a_{21} = 1.52*10^{-7} cm^{-2}s^{-1}$$
$$a_{22} = 6.08*10^{-7} cm^{-2}s^{-1}$$
$$a_{24} = 1.22*10^{-9} cm^{-2}s^{-1}$$
$$b_{22} = b_{23} = b_{24} = b_{26} = 14V^{-1}$$

Case 3 parameters

$$a_{21} = 1.9*10^{-9} cm^{-2}s^{-1}$$
$$a_{23} = 2*10^{-7} cm^{-2}s^{-1}$$
$$b_{22} = b_{23} = b_{24} = b_{26} = 14V^{-1}$$
$$b_{20} = 18V^{-1}$$

In the case of Case2 and Case 3 parameters, the values except those shown were the same as in Case 1 parameters.

Results and Discussion: Figure 1 presents the concentration dependence of the electroactive species on the pH of the bath. The plot shows that before pH 6.5, the electroactive species are completely dissolved in the bath and that the major part of Ni remains as Ni^{2+}. The concentration of $Ni(OH)^{+}$increases logarithmically with pH. After pH 6.5, the concentration of Ni^{2+} and $Ni(OH)^{+}$ reduce drastically, and almost all the nickel is precipitated as $Ni(OH)_2$. So, it is apparent from the plot that the bath becomes unstable after a pH of 6.5, and that it is essential to keep the pH level below 6.5.

Evan's diagram was constructed to understand the thermodynamics of nickel deposition process along with hydrogen evolution as a parasitic reaction. The Evans diagram was obtained for both nickel reduction and the hydrogen evolution process. The values of 'a' and 'b' were found from literature[1], and the potentials were plotted as a function of log i using the given relations. Figure 2 presents the Evans diagram for nickel reduction and hydrogen evolution in a Watt's bath. The potential shown in the plot is with respect to the Standard Hydrogen Electrode (SHE). The plot shows that the equilibrium potential for nickel is –0.25 V. The equilibrium potential for hydrogen is 0 V. The plot also shows that the equilibrium exchange current density of hydrogen is almost one order of magnitude lesser than that of nickel. As seen from Figure 2, for a given overpotential, the partial current density due to hydrogen evolution is at least one order of magnitude higher than that of nickel reduction. In other words, thermodynamics favor more hydrogen evolution than nickel deposition. Ideally no amount of Ni deposition can take place in aqueous electrolytes since most of the current goes towards hydrogen evolution according to Figure 2. In practice the overpotential for hydrogen evolution is larger than that shown in

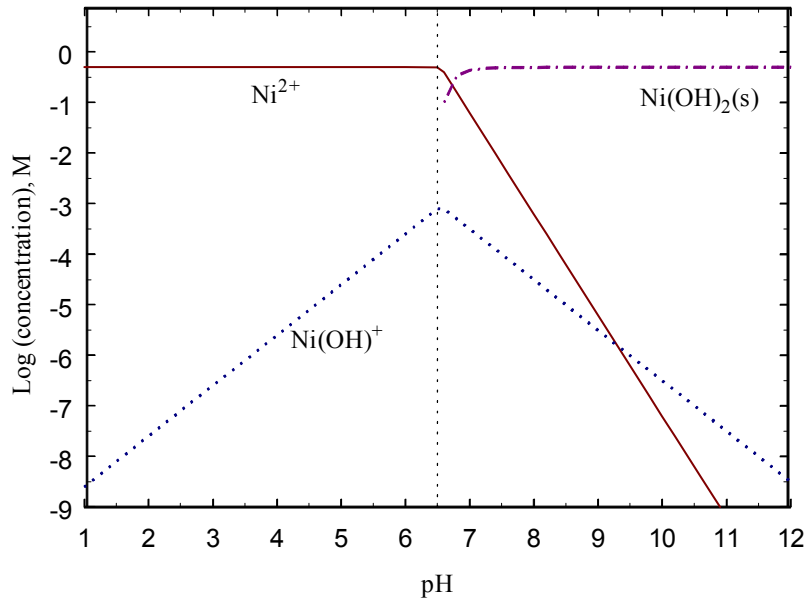

Figure 1. Change in concentrations of electroactive species with bath pH

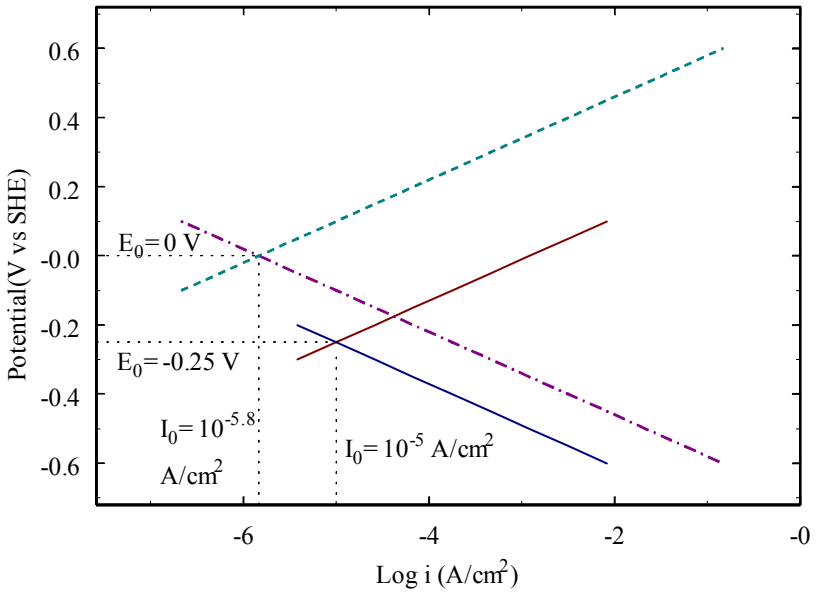

Figure 2. Evans diagram for Ni-H_2 system

Fig. 2 and hence Ni deposition proceeds at acceptable rates. However, the current efficiency for nickel deposition is much lower than 100% due to hydrogen evolution.

The adsorption model simulations were aimed at understanding the relative kinetics of the two competing cathodic reactions. With the adsorption model, the change in the parameters (from Case 1 to Case 2 etc.) has an effect of decreasing the pH of the electrolyte[2]. Figure 3 gives the surface coverages of the two adsorbed species (Ni^{+}_{ads} and H_{ads}) under the given simulation conditions. As seen from the plot, for Case 1, we can see that the electrode surface is mainly covered by hydrogen ad-atoms. A decrease in the pH is seen to decrease the concentration of H_{ads} on the electrode surface and increase the concentration of Ni^{+}_{ads}. This result would directly translate into an increase in the coulombic efficiency for the Ni deposition process, as the predominance of the Ni^{+}_{ads} species is a pre-requisite for Ni deposition. However, a further decrease in pH again increases the surface concentration of H_{ads}, which is to be expected considering that Ni^{+}_{ads} also acts as a catalyst for H_{ads} production. Further, in all the cases, the surface coverage of the Ni^{+}_{ads} species increases and that of H_{ads} decreases with an increase in the overpotential. This trend is seen to cease when the overpotential reaches a value greater than 0.8 V. A further increase in overpotential does not increase the concentration of Ni^{+}_{ads}, indicating that the overpotential range of 0.6-0.8 V gives the best coulombic efficiency. Further studies need to be done to understand the reason for the changes in the concentration of the adsorbed species on the electrode surface with a change in deposition conditions.

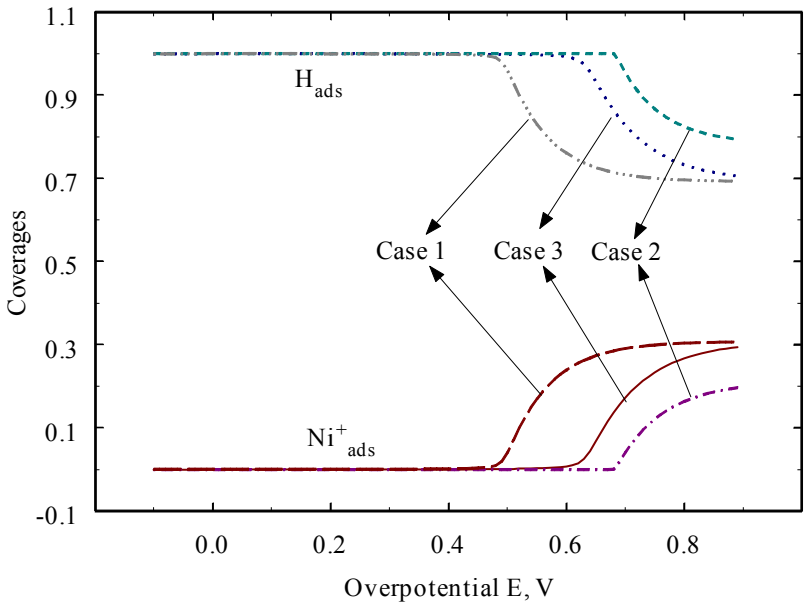

Figure 3. Dependence of Surface coverage of adsorbed species with overpotential

The steady-state solution of equations 20-22 gives the polarization curves. Figure 4 gives the variation in the current density as a function of the overpotential used. We can see from the plot that the current density decreases from case 1 to case 3. As explained from

figure 3, case 2 gives the optimal surface coverage of the Ni^{+}_{ads}. Again, in the polarization curve also shows the least current for a given overpotential for case 2 parameters. This result indicates that the increased current density values seen in Case 1 and Case 3 is utilized mainly for hydrogen evolution reaction. The increased hydrogen

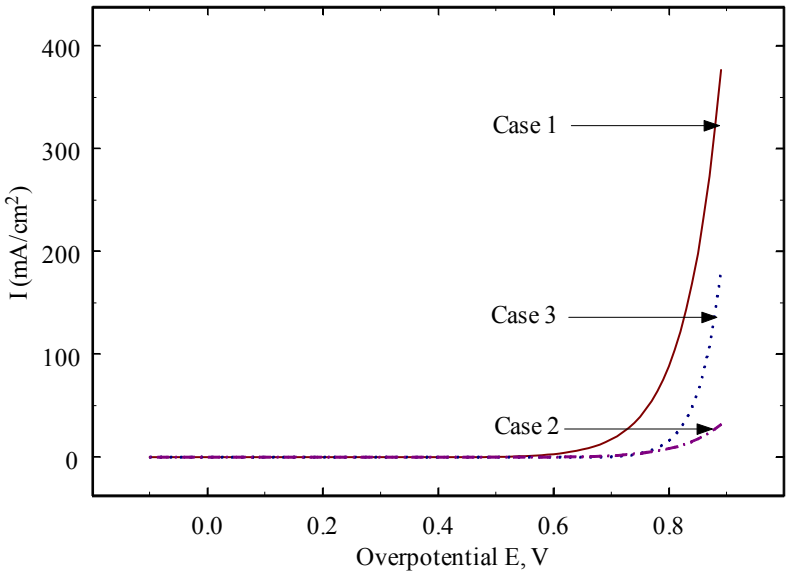

Figure 4. Dependence of Current density with overpotential

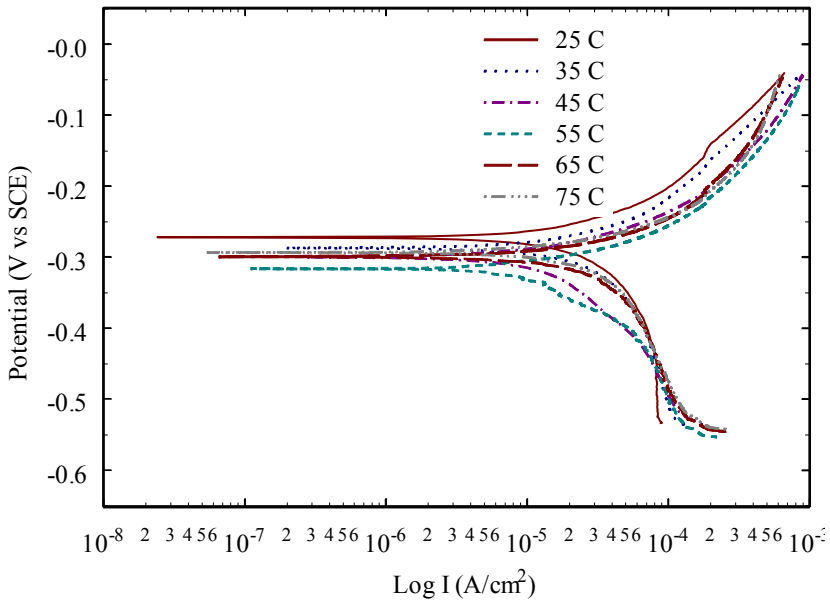

Figure 5. Tafel Polarization studies of Ni deposition from Watts bath at different temperatures

evolution reaction would lead to a decrease in the current efficiency for the deposition process, which again corroborates the results found in Figure 3. However, it must be mentioned that the reason for the presence of an optimal pH for the deposition process has to be explored to understand the mechanism of Ni deposition process in sulfate electrolytes.

Effect of Temperature: Tafel polarization studies were done for the deposited nickel under the bath conditions. Figure 5 gives the Tafel plots of the deposited nickel at various temperatures. According to the Evan's diagram shown in Figure 2, a plot of E *vs.* log I should yield a straight line with the slope equal to the Tafel constant. However, the Tafel plots in Figure 3 reveal two different Tafel slopes. At low to moderate overpotentials, one slope is observed. At high overpotentials a different slope is observed. The Tafel slope at low overpotentials can be attributed to Ni deposition and dissolution. The Tafel slopes at high overpotentials are due to the hydrogen evolution/oxidation reaction. Current studies are focused on obtaining the parameters that characterize the kinetics involved in both these processes.

Figures 6a and 6b present the cyclic voltammograms (CVs) obtained at various temperatures at a scan rate of 1 mV/s. The CVs were done by sweeping the potential from –0.15 V to –0.8 V in the forward scan and then back from –0.8 V to –0.15 V in the reverse scan. The sweep rate was kept the same during both forward and reverse scans. During the forward sweep from –0.15 V to –0.8, both Ni deposition and hydrogen evolution occur. Since, the solution contains excess H^+ ions hydrogen evolution is not rate limited. This is seen by the rapid increase in current density beyond –0.65 V in Figure 6a. The plot also shows that hydrogen evolution does not begin at –0.25 V (0 V *vs*. SHE) as predicted by the Evan's diagram (Figure 2). This is due to the overpotential for hydrogen evolution on the copper substrate. Hence, at low temperatures we observe a reduction peak, which corresponds to Ni deposition. However, this peak vanishes with increase in temperature. This can be attributed to the enhancement of the hydrogen evolution reaction with temperature. Hydrogen evolution masks the Ni deposition reaction and hence the reduction peaks cannot be seen clearly.

During the reverse sweep from –0.8 V to –0.15 V, two peaks are seen at different temperatures. The first peak corresponds to that of Ni dissolution and the second peak to that of adsorbed hydrogen oxidation. Since a limited amount of hydrogen is adsorbed on the surface, a clear peak appears during the forward scan. Increasing the temperature increases the kinetics for both Ni reduction/oxidation and hydrogen evolution/oxidation.

References:

1. L. I. Antropov, *Theoretical Electrochemistry*, Mir publishers, Moscow (1972).
2. I. Epelboin, M. Joussellin, R. Wiart, *J. Electroanal. Chem.*, **119**, 61 (1981).

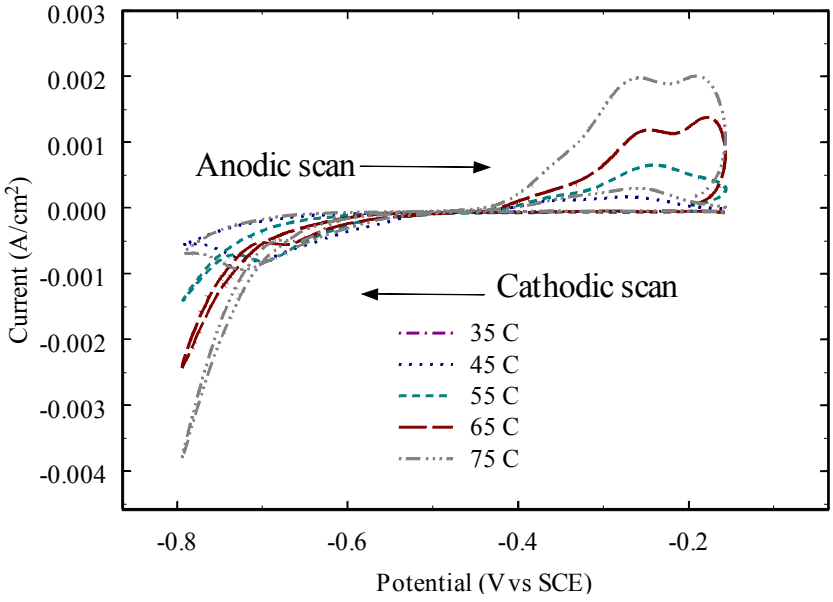

Figure 6a. Cyclic Voltammograms of Ni deposition from Watts bath at different temperatures

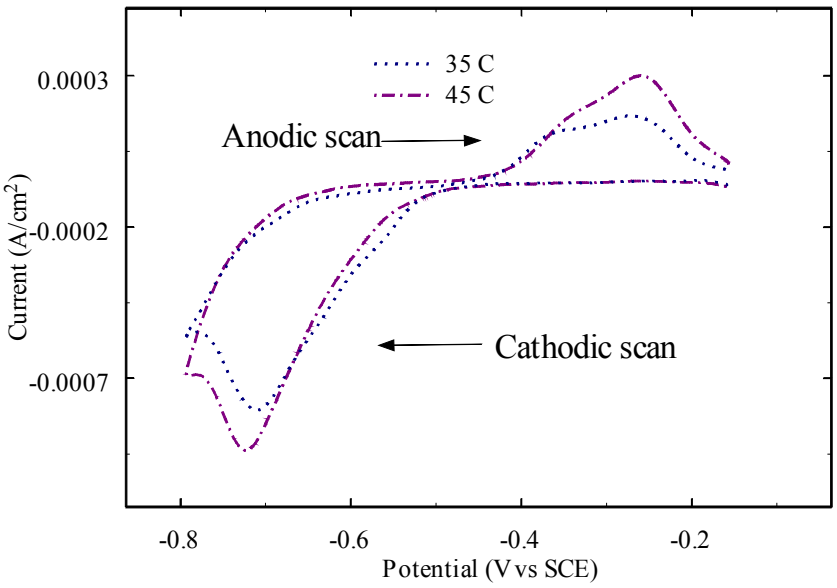

Figure 6b. Cyclic Voltammograms of Ni deposition from Watts bath at different temperatures.

7 DISTRIBUTION

MS 0384	9140	H. S. Morgan
MS 0825	9110	W. H. Hermina
MS 0826	9113	S. N. Kempka
MS 0826	9113	D. R. Noble
MS 0826	9113	P. A. Sackinger
MS 0826	9113	C. C. Wong
MS 0826	9114	J. E. Johannes
MS 0826	9114	T. A. Baer
MS 0826	9114	K. S. Chen (5)
MS 0826	9114	H. K. Moffat
MS 0826	9114	R. R. Rao
MS 0826	9114	P. R. Schunk
MS 0826	9114	A. C.-T. Sun
MS 9404	8750	G. D. Kubiak
MS 9042	8750	S. K. Griffiths
MS 9401	8751	D. M. Skala
MS 9042	8752	C. D. Moen
MS 9042	8752	G. H. Evans (2)
MS 9042	8752	R. S. Larson
MS 9042	8752	R. H. Nilson
MS 9042	8752	A. Ting
MS 9401	8753	G. F. Cardinale
MS 9401	8753	J. J. Kelly
MS 9401	8753	D. R. Boehme
MS 9409	8754	S. H. Goods
MS 9403	8762	L. A. Domeier
MS 9403	8762	A. M. Morales
MS 9403	8773	N. Y. C. Yang
MS 0311	2618	R. Wild
MS 0619	12690	Review and Approval Desk (2) for DOE/OSTI
MS 0899	4916	Technical Library (2)
MS 9018	8940-2	Central Technical Files

Honeywell FM&T
P. O. Box 419159
Kansaa City, MO 64141-6159

MS 1C41	R. Steinhoff
MS MD40	M. Widmer
MS MD40	K. Mandl

Prof. Branko N. Popov
Department of Chemical Engineering
University of South Carolina
Columbia, SC 29209

Prof. Ralph Greif
Department of Mechanical Engineering
University of California, Berkeley
Berkeley, CA 94720